

Author Manuscript

This is the author manuscript accepted for publication and has undergone full peer review but has not been through the copyediting, typesetting, pagination and proofreading process, which may lead to differences between this version and the [Version of Record](#). Please cite this article as [doi: 10.1111/jmg.12211](https://doi.org/10.1111/jmg.12211)

This article is protected by copyright. All rights reserved

1 **Activity–composition relations for the calculation of**
2 **partial melting equilibria in metabasic rocks.**

3 E. C. R. Green^{1*}, R. W. White², J. F. A. Diener³, R. Powell⁴,
4 T. J. B. Holland⁵ and R. M. Palin²

5 ¹*Institute of Geochemistry and Petrology, ETH Zurich, Clausiusstrasse 25, 8092 Zurich,*
6 *Switzerland (eleanor.green@erdw.ethz.ch)*

7 ²*Institute of Geosciences, Johannes Gutenberg University of Mainz, 55128 Mainz, Germany*

8 ³*Department of Geological Sciences, University of Cape Town, Rondebosch 7701, South*
9 *Africa*

10 ⁴*School of Earth Sciences, University of Melbourne, Victoria 3010, Australia*

11 ⁵*Department of Earth Sciences, University of Cambridge, Cambridge, CB2 3EQ, UK*

12 *Corresponding author

13 Short title: $A-x$ relations for metabasic rocks

14 **ABSTRACT**

15 A set of thermodynamic models is presented that, for the first time, allows partial melting
16 equilibria to be calculated for metabasic rocks. The models consist of new
17 activity–composition relations combined with end-member thermodynamic properties from
18 the Holland & Powell dataset, version 6. They allow for forward modelling in the system
19 $\text{Na}_2\text{O}–\text{CaO}–\text{K}_2\text{O}–\text{FeO}–\text{MgO}–\text{Al}_2\text{O}_3–\text{SiO}_2–\text{H}_2\text{O}–\text{TiO}_2–\text{Fe}_2\text{O}_3$. In particular, new
20 activity–composition relations are presented for silicate melt of broadly
21 trondhjemitic–tonalitic composition, and for augitic clinopyroxene with Si–Al mixing on the
22 tetrahedral sites, while existing activity–composition relations for hornblende are extended
23 to include K_2O and TiO_2 . Calibration of the activity–composition relations was carried out
24 with the aim of reproducing major experimental phase-in/phase-out boundaries that define
25 the amphibolite–granulite transition, across a range of bulk compositions, at ≤ 13 kbar.

26 **Key words:** amphibolite; granulite; calibration; pseudosection; Holland & Powell dataset.

27 INTRODUCTION

28 The introduction in recent decades of forward modelling via calculated phase diagrams (e.g.
29 Powell & Holland, 1988; Powell *et al.*, 1998) represents a major development in
30 metamorphic petrology. Suitable phase diagrams, commonly known as pseudosections, map
31 the equilibrium phase assemblages subject to constraints of bulk composition, usually in
32 pressure–temperature (P – T), temperature–bulk composition (T – X) or pressure–bulk
33 composition (P – X) space. To produce such diagrams, the thermodynamics of each of the
34 phases involved must be described by a model. A model consists of one or more
35 end-members, with thermodynamic properties typically taken from an internally-consistent
36 thermodynamic dataset. For multiple-end-member phases, such as solid solutions, the
37 end-member properties must be combined with activity–composition (a – x) relations
38 describing the thermodynamics of mixing of the end-members.

39 End-member thermodynamic datasets in current use include those of Holland & Powell
40 (most recently Holland & Powell, 2011), Berman (1988), Gottschalk (1996) and Chatterjee
41 *et al.* (1998). The development of model a – x relations for minerals and melts has a long
42 history, with much early work having the purpose of generating thermodynamically-based
43 thermometers and barometers (e.g. Wood & Banno, 1973; Stormer, 1975; Thompson, 1976;
44 Newton & Haselton, 1981). Model a – x relations are almost inevitably under-constrained by
45 the available data, and so, when the aim is to calculate phase diagrams, it is sensible to
46 select a – x relations for the various phases that have been parameterised to work together as
47 a set. In this way, deficiencies in the thermodynamic model for one phase may compensate
48 for those in the model for another phase, producing appropriate stable assemblages overall.
49 Widely used sets of a – x relations include those developed for the modelling of metapelitic
50 or ultramafic rocks based on the Holland & Powell (1998, 2011) datasets (e.g. White *et al.*,
51 2007, 2014; Chu & Ague, 2013; Holland *et al.*, 2013; Klemme *et al.*, 2009), and those
52 incorporated into the MELTS software and its extensions pMELTS, pHMELTS and

53 rhyolite-MELTS, for modelling of partial melting equilibria in ultramafic and felsic systems
54 (Smith & Asimow, 2005; Ghiorso & Sack, 1995; Ghiorso *et al.*, 2002; Asimow *et al.*, 2004;
55 Gualda *et al.*, 2012).

56 Until now, no set of a - x relations has been available for the modelling of partial melting
57 equilibria in metabasic rocks. The current MELTS, pMELTS and rhyolite-MELTS models
58 are not intended to calculate equilibria between melt and amphibole or biotite. A - x
59 relations by e.g. Coggon & Holland (2002); Diener *et al.* (2007); Green *et al.* (2007); Diener
60 & Powell (2012), founded on the superceded Holland & Powell (1998) dataset, allow
61 modelling of subsolidus metabasic rocks up to amphibolite and eclogite facies. However,
62 there is no corresponding model for the melt phase; the metapelite melt model of Holland &
63 Powell (2001) and White *et al.* (2007, 2014) is not parameterised for any but peraluminous,
64 K_2O -rich, CaO -poor felsic melt compositions. Moreover, the a - x relations for several key
65 solid phases are not appropriate for use at granulite-facies temperatures: the hornblende
66 model of Diener *et al.* (2007) omits K_2O and TiO_2 , while the clinopyroxene model of Green
67 *et al.* (2007) does not allow for Al on the tetrahedral site, or for Mg or Fe^{2+} on the M2-site.

68 Our new work fills these gaps. In this paper we provide a - x relations for broadly
69 tonalitic-trondjhemitic silicate melt, high-temperature augitic clinopyroxene, and
70 K-,Ti-bearing hornblende, representing revision and substantial extension of previous
71 models. Other phases that are required for the modelling also appear in metapelitic
72 equilibria, and we have taken the relevant a - x relations from the set of White *et al.* (2014).
73 The two sets of a - x relations therefore overlap. As a set, the thermodynamic models for
74 metabasite melting equilibria are formally calibrated to 13 kbar, and should be used at
75 higher pressures only with sceptical assessment of the results. The 13 kbar limit was
76 imposed due to the lack of a thermodynamic model for aqueous fluid containing a significant
77 proportion of dissolved silicate material, and was inferred from experimental and modelling
78 work on the solubility of silicate minerals (Manning, 1994; Gerya *et al.*, 2005; Manning,
79 2007; Newton & Manning, 2008; Dolejš & Manning, 2010; Hunt & Manning, 2012).

80 This paper presents the development and calibration of the new $a-x$ relations, while in
81 a companion paper (Palin *et al.*, 2016b, this issue), we examine their application to forward
82 modelling in a range of basic to intermediate bulk compositions. Calibration of the $a-x$
83 relations ultimately made use of experiments in natural systems, modelled in the system
84 $\text{Na}_2\text{O}-\text{CaO}-\text{K}_2\text{O}-\text{FeO}-\text{MgO}-\text{Al}_2\text{O}_3-\text{SiO}_2-\text{H}_2\text{O}-\text{TiO}_2-\text{Fe}_2\text{O}_3$ (NCKFMASHTO). A large
85 body of experimental work has explored phase relations in partially molten metabasic rocks,
86 frequently seeking to determine the origins of tonalite-trondhjemite-granodiorite (TTG)
87 magmas (e.g. Beard & Lofgren, 1991; Rapp *et al.*, 1991; Rushmer, 1991; Sen & Dunn, 1994;
88 Wolf & Wyllie, 1994; Patiño Douce & Beard, 1995; Rapp & Watson, 1995; Skjerlie & Patiño
89 Douce, 1995; Springer & Seck, 1997; López & Castro, 2001; Skjerlie & Patiño Douce, 2002;
90 Foley *et al.*, 2003; Auzanneau *et al.*, 2006; Qian & Hermann, 2013; Zhang *et al.*, 2013; Ziaja
91 *et al.*, 2014). During the calibration process, for a subset of the experimental studies,
92 forward calculations of phase relations at the experimental bulk compositions were
93 compared with the observations. The primary goal was to reproduce major
94 phase-in/phase-out boundaries, which, it is hoped, ensures that the behaviour of the models
95 will be broadly realistic in the forward-modelling context for which they are intended.

96 GENERAL NOTES ON THE THERMODYNAMIC MODELS

97 The set of $a-x$ relations presented here will be referred to as the ‘metabasite set’. It is
98 suitable for use with versions 6.2 or 6.3 of the Holland & Powell (2011) dataset (ds62, ds63),
99 created 6 February 2012 and 15 January 2015 respectively. The figures in this paper were
100 calculated with version 6.2. The update to version 6.3 includes a key refinement to the
101 thermodynamics of the H_2O end-member in the melt, and is expected to give slightly more
102 realistic results at the wet solidus. In other respects, differences between calculations with
103 ds62 and ds63 are believed to be insignificant. The $a-x$ relations should not however be

104 expected to give meaningful output with the older, widely used version 5.5 (ds55) of the
105 dataset (Holland & Powell, 1998); indeed ds55 lacks one of the necessary melt
106 end-members. Full descriptions of the $a-x$ relations of the metabasite set appear in the
107 Appendix, along with a guide to downloading the files necessary for using them via the
108 software THERMOCALC (Powell & Holland, 1988). Calculations in this paper were carried
109 out with THERMOCALC, version tc340i.

110 This paper will refer to two existing groups of $a-x$ relations used for calculations on
111 metapelitic rocks. The first, the metapelite ‘ds55-set’, was published by White *et al.* (2007)
112 for use with version 5.5 of the Holland & Powell dataset (created 22 November 2003), and
113 has since been slightly modified. The second, the metapelite ‘ds6-set’, was a major revision
114 of the same models for version 6.1 of the dataset (created 13 November 2011), by White
115 *et al.* (2014).

116 Abbreviations for the names of end-members are consistent with the Holland & Powell
117 dataset, and are either explained in the text or defined in the Appendix. End-members that
118 are treated as pure phases are quartz (q), albite (ab), sphene (sph), rutile (ru), and
119 lawsonite (law). The following solution phases appear in the text and figures: actinolite
120 (act), glaucophane (gl), hornblende (hb), orthopyroxene (opx), garnet (g), plagioclase (pl,
121 $C\bar{1}$, and $pl_1, I\bar{1}$, the latter used for comparison with experiments where $x^{\text{an}} > 0.8$),
122 potassium feldspar (ksp), biotite (bi), muscovite (mu), chlorite (chl), silicate melt (L),
123 epidote (ep), ilmenite (ilm), magnetite (mt), and olivine (ol). Additionally five
124 clinopyroxene (cpx) phases are referred to, represented with two different sets of $a-x$
125 relations. Augitic clinopyroxene (aug) and pigeonite (pig) are considered to have the
126 general formula $[\text{Ca}, \text{Na}, \text{Mg}, \text{Fe}^{2+}]^{\text{M2}} [\text{Mg}, \text{Fe}^{2+}, \text{Al}, \text{Fe}^{3+}]^{\text{M1}} [\text{Si}, \text{Al}]_2^{\text{tet}}$, while diopside (di),
127 jadeite (jd) and omphacite (o) have the general formula $[\text{Ca}, \text{Na}]^{\text{M2}} [\text{Mg}, \text{Fe}^{2+}, \text{Al}, \text{Fe}^{3+}]^{\text{M1}}$
128 Si_2^{tet} , with omphacite forming via order-disorder on the M sites.

129 Among these phases, the $a-x$ relations for metabasite melt (L), augitic clinopyroxene

130 (aug and pig) and clinoamphibole (hb, gl and act) are newly calibrated to address partial
131 melting of metabasitic rocks. Of the clinoamphiboles, only hornblende is normally relevant
132 to supersolidus amphibolite–granulite facies conditions, but the new amphibole a – x model
133 is also appropriate for actinolite and glaucophane at lower temperatures. The remaining
134 a – x models in the metabasite set, for the phases garnet, orthopyroxene, feldspar,
135 spinel–magnetite and ilmenite, were taken from the metapelite ds6-set.

136 Additionally, the existing a – x model for the potentially ordered sodic–calcic pyroxenes
137 jd, di and o (from Green *et al.*, 2007, for use with ds55), has been updated for use with ds6
138 of the Holland & Powell dataset (Holland & Powell, 2011). This model, the ‘omphacite’
139 model, remains the appropriate clinopyroxene model to use under subsolidus conditions
140 where co-existing clinopyroxenes might occur. It should not be used in calculations that
141 also involve the augitic clinopyroxene model.

142 **Form of the a – x relations**

143 Like the metapelite ds55- and ds6-sets, the a – x relations developed in this paper are
144 macroscopic regular solution models, in which non-ideal enthalpic interactions are present
145 between pairs of end-members, expressed as interaction energies $W_{i,j}$. The mixing-on-sites
146 approach is adopted, in order to give an approximately correct form for the ideal entropy of
147 mixing. The regular solution paradigm is modified by allowing the $W_{i,j}$ in principle to be
148 linear functions of P and T , though in practice it is almost never possible to resolve these
149 two dependencies, and the $W_{i,j}$ are usually treated as constant or functions of P only. The
150 formulation is discussed extensively by Powell & Holland (1993) and Holland & Powell
151 (1996a,b), under the name ‘symmetric formalism’. A further modification, the asymmetric
152 formalism (Holland & Powell, 2003), introduced asymmetry in the manner of van Laar
153 (1906) via ‘volume’ parameters, α_i , associated with each end-member i .

154 In the symmetric formalism, non-ideal contributions to the enthalpy of mixing are

155 introduced via activity coefficients written as

$$156 \quad RT \ln \gamma_l = - \sum_i^{n-1} \sum_{j>i}^n (p'_i - p_i)(p'_j - p_j) W_{i,j}, \quad (1)$$

157 where γ_l is the non-ideal activity coefficient of end-member l , T is the temperature, R is the
158 gas constant, p_k is the proportion of end-member k in the phase, p'_k is the value of p_k in
159 end-member l , such that $p'_k = 1$ where $k = l$ and $p'_k = 0$ where $k \neq l$, and the n
160 end-members in the phase form an independent set. In the asymmetric formalism, the
161 non-ideal contributions are written

$$162 \quad RT \ln \gamma_l = - \sum_i^{n-1} \sum_{j>i}^n (\phi'_i - \phi_i)(\phi'_j - \phi_j) W_{i,j} \left(\frac{2\alpha_i}{\alpha_i + \alpha_j} \right), \quad (2)$$

163 where ϕ_i is the proportion of end-member i weighted by the van Laar parameters,
164 $\phi_i = (p_i \alpha_i) / (\sum_k^n p_k \alpha_k)$, and ϕ'_i is likewise the van Laar-weighted equivalent of p'_i .

165 The free parameters available for fitting are therefore the $W_{i,j}$ and α_i values. In
166 addition, it is sometimes necessary to introduce an expression ΔG_i , which represents an
167 adjustment to the Gibbs energy of end-member i relative to its function $G_i(P, T)$ in the
168 dataset. The ΔG_i take the form $a + b T + c P$. ΔG_i expressions were introduced into the
169 metabasite set for a number of reasons:

- 170 • ΔG_i^{od} represents the ΔG of ordering. It is applied to an end-member that represents
171 full ordering of cations on sites, at an intermediate composition. It captures the
172 enthalpy change of formation of the ordered intermediate end-member, when it is
173 made by reaction of the end-members at the compositional extremes.
- 174 • ΔG_i^{mod} . This is a modification made to the thermodynamics of a dataset end-member
175 simply in order to improve the behaviour of the $a-x$ relations in phase diagram
176 calculations. A non-zero value may imply that the dataset thermodynamic data for
177 the relevant end-member might be inappropriate, or just that the end-member is
178 accommodating various other deficiencies in the thermodynamic models.

- 179 • ΔG_i^{make} . Certain minor or ‘fictive’ end-members in the $a-x$ models do not appear in
180 the dataset. To approximate their $G_i(P, T)$ functions, a linear combination of dataset
181 end-members is chosen that produces the right composition. The $G(P, T)$ functions of
182 these end-members are combined likewise, and a ΔG_i^{make} expression is added that can
183 be calibrated to represent the ΔG between the combination of dataset end-members
184 and the fictive end-member.
- 185 • ΔG_i^{tran} . This is a special case of ΔG_i^{make} , in which a first order phase transition
186 separates end-member i from dataset end-member j of the same composition but
187 different symmetry. Then ΔG_i^{tran} represents ΔG of the $i-j$ transition.

188 Examples of all of these appear in the $a-x$ relations in the Appendix.

189 This paper adopts the following notational conventions: (1) as $W_{i,j} \equiv W_{j,i}$, either
190 notation may be used for a given pair of end-members; (2) the interaction energies between
191 an end-member i and multiple, specified end-members j, k, \dots in the same phase are
192 represented as $W_{i,[j,k,\dots]}$; (3) the expression $W_{i,n}$, or $W_{iL,nL}$ for the liquid model, represents
193 the set of $W_{i,j}$ parameters between end-member i and all of the other end-members in the
194 same $a-x$ model.

195 Calibration strategy

196 The root of the calibration approach was the fitting of key parameters in small,
197 well-constrained chemical subsystems. Thus, each of the new $a-x$ models has a core in a
198 major subsystem that was developed independently of the other new models. The models
199 were then completed sequentially. First the augite model was developed entirely in
200 amphibole-free and melt-free assemblages. Then the clinoamphibole model was completed
201 based on calculations in which the augite model was treated as fixed. Finally, both the
202 augite and clinoamphibole $a-x$ relations were treated as fixed, while the melt model was
203 completed based on observations from a selection of experimental studies on

204 TTG-generation. The choice of TTG-generation studies was limited to those with multiple
205 hydrate-breakdown melting runs at ≤ 13 kbar, placing constraints on significant
206 phase-in/phase-out boundaries, with bulk compositions that could reasonably be modelled
207 in NCKFMASHTO (for example, they should be nominally carbon-free).

208 In general (for variance > 2), the calculations performed during the calibration process
209 mimicked those performed when the finished models are used; they were forward
210 calculations that gave the compositions and modal proportions of phases at equilibrium,
211 subject to the constraint of the experimental bulk composition. In some cases the
212 calculations took place at the P - T conditions of an experiment, for direct comparison with
213 the experimental run products. However, the highest priority for the calibration was to
214 make good predictions of the major features of phase relations across P - T space, rather
215 than to make accurate predictions of phase compositions. Consequently, the interpolated
216 positions of key phase field boundaries (e.g. orthopyroxene-in, hornblende-out) were used
217 directly in calibration. The final step in calibration was to calculate full P - T
218 pseudosections for key experimental bulk compositions, ensuring that the assemblages
219 specified during the calibration were the most stable that could be modelled.

220 Calibrations that are new in this work were carried out either by manual trial and error
221 or by using a Monte Carlo method, MCTC, within the THERMOCALC software. When MCTC
222 is invoked, THERMOCALC calculates a set of phase equilibria repeatedly, using a - x models
223 with parameters drawn randomly from within specified distributions. ‘Successful’ sets of
224 model parameters are identified by comparing the resulting calculated phase equilibria with
225 the observations, and the distribution of successful model parameters is reviewed, leading to
226 refinement of the initial distribution. Over the course of many MCTC runs, the user will first
227 widen the initial distributions of model parameters until, for each parameter, a peak is
228 visible in the distribution of successful values. Then, certain model parameters may be
229 given fixed values, especially those that are weakly constrained (their ‘successful’
230 distributions are wide), or strongly correlated with other parameters. The distributions of

231 all parameters are narrowed over time, with the aim of deriving quasi-optimised values.

232 The MCTC approach is thus a hybrid between manual trial and error and a formal,
233 automated technique. It robustly handles two problems: the very high and
234 multi-dimensional correlations among successful distributions of model parameters, and the
235 presence of parameters that are essentially unconstrained by the data. A fitting method that
236 does not take these phenomena into account is at risk of generating physically implausible
237 parameter values, leading to a - x relations that do not extrapolate well in P - T - X space.

238 In order to use phase equilibrium experiments as constraints, it is necessary to infer
239 bulk compositions that represent the experimental run products at equilibrium. Two
240 components of bulk composition in particular are hard to estimate: those of fluid content,
241 assumed to be all water ('molar bulk H_2O ', $M_{\text{H}_2\text{O}}$), and of oxygen ('molar bulk O', M_{O}).
242 Experimental studies routinely provide estimates of H_2O content in the starting material,
243 though these are uncertain, and unlikely to include H_2O gained by adsorption during the
244 pulverisation of the sample, which may be retained even during storage under desiccation
245 (London *et al.*, 2012). M_{O} may be equated directly to molar bulk Fe_2O_3 , via the reaction
246 $\text{Fe}_2\text{O}_3 = 2 \text{FeO} + \text{O}$, if iron is the only element considered to have variable oxidation state.
247 The fraction of iron present as Fe_2O_3 in the starting material is rarely estimated. During
248 experimental runs, values of $M_{\text{H}_2\text{O}}$ and M_{O} in the capsule are subject to interdependent
249 changes. The experiments considered in this work were not formally buffered to specified
250 f_{O_2} , but even in such cases, the experimental apparatus has an 'intrinsic f_{O_2} ' that
251 influences the oxidation state of the starting material during the run; hence M_{O} is not
252 conserved. The process of oxidation or reduction of starting materials primarily involves
253 diffusion of H_2 , to which experimental capsules are effectively open. If the apparatus
254 provides an environment that is reducing with respect to the oxidation state of the starting
255 materials, H_2 will enter the capsule and may form H_2O by reduction of iron oxides,
256 constituting an increase in $M_{\text{H}_2\text{O}}$ and decrease in M_{O} (carbon, derived from graphite
257 furnaces, may play a under-acknowledged role in this process; see Brooker *et al.*, 1998;

258 Jakobsson, 2012; Matjuschkin *et al.*, 2015). Finally, apparent loss or gain of both H₂ and
259 O₂, or possibly molecular H₂O, has been reported in several piston cylinder studies (e.g.
260 Patiño Douce & Beard, 1994, 1995; Truckenbrodt & Johannes, 1999; Pichavant *et al.*, 2002;
261 Jakobsson, 2012), especially during longer and higher-temperature experiments.

262 There is therefore no satisfactory way to convert the information reported in an
263 experimental study into values of M_{O} and $M_{\text{H}_2\text{O}}$ suitable for a representative pseudosection.
264 A crucial part of the model calibration, then, is to analyse the sensitivity of calculations to
265 the assumed values of M_{O} and $M_{\text{H}_2\text{O}}$. This is done most informatively by calculating T - X
266 or P - X pseudosections, in which X is M_{O} or $M_{\text{H}_2\text{O}}$.

267 CLINOPYROXENE A - X RELATIONS

268 Omphacite model

269 The ‘omphacite model’ of Green *et al.* (2007), modified by Diener & Powell (2012), was
270 developed with the aim of modelling coexisting jadeite–omphacite and omphacite–diopside
271 pairs. Previously calibrated with ds55, it was upgraded in this work for use with version 6
272 of the Holland & Powell dataset. It remains the only appropriate choice of a - x relations
273 wherever diopsidic and sodic clinopyroxenes may stably coexist, since the new augitic
274 clinopyroxene model is intended for use at temperatures higher than the closure of the
275 jadeite–omphacite and omphacite–diopside miscibility gaps, and has no capacity to
276 represent the ordered omphacite structure.

277 The omphacite model allows for cation mixing as $[\text{Mg}, \text{Fe}^{2+}, \text{Al}, \text{Fe}^{3+}]^{\text{M1}}$ and $[\text{Ca},$
278 $\text{Na}]^{\text{M2}}$, but in order to represent ordered intermediate end-members such as omphacite
279 $(\text{Ca}_{\frac{1}{2}}^{\text{M2}}\text{Na}_{\frac{1}{2}}^{\text{M2}}\text{Mg}_{\frac{1}{2}}^{\text{M1}}\text{Al}_{\frac{1}{2}}^{\text{M1}}\text{Si}_2^{\text{tet}}\text{O}_6)$, it treats the M1 and M2 sites as ‘split’. That is, Mg, Fe²⁺,
280 Al and Fe³⁺ mix on a M1m and a M1a site, with cations preferentially partitioned onto the

281 M1m site in the order $\text{Fe}^{2+} > \text{Mg} > \text{Al} > \text{Fe}^{3+}$, while Ca and Na mix on a M2c and a M2n site,
282 with Ca preferentially partitioned onto M2c (Green *et al.*, 2007). The tetrahedral sites
283 contain Si only.

284 Slight modifications were needed in order to compensate for the change from version 5.5
285 to version 6 of the dataset. Following Diener & Powell (2012), modifications were made
286 simultaneously for both the omphacite model, and the NCFMASHO core of the ds55
287 clinoamphibole model of Diener *et al.* (2007; refined by Diener & Powell, 2012). For the
288 omphacite model, the modification amounted to a change in $\Delta G_{\text{acm}}^{\text{mod}}$ on the acmite
289 end-member, from -4 to -7 kJ. The change was determined by manually adjusting the
290 ΔG_i^{mod} values of end-members in both models, until satisfactory calculations were obtained
291 for equilibria in a MORB-like composition (composition Mcal, Table 1, H_2O in excess).

292 The $W_{i,j}$ parameters were left unchanged from the previous version of the omphacite
293 model, since these were relatively well constrained by the observed geometry of the solvi
294 between the diopsidic, omphacitic and jadeitic portions of the solid solution. Conversely,
295 since the solvi depend solely on the mixing properties of the models, rather than the
296 end-member thermodynamics, solvus calculations will be unchanged from the previous
297 model.

298 **Augite model**

299 Prompted by the compositions of clinopyroxene in TTG-genesis experiments (e.g. Patiño
300 Douce & Beard, 1995; Skjerlie & Patiño Douce, 2002; Rapp & Watson, 1995), a new ‘augite
301 model’ was developed for calcic clinopyroxene at high temperature, with mixing on sites as
302 $[\text{Mg}, \text{Fe}^{2+}, \text{Al}, \text{Fe}^{3+}]^{\text{M1}} [\text{Ca}, \text{Na}, \text{Mg}, \text{Fe}^{2+}]^{\text{M2}} [\text{Si}, \text{Al}]_2^{\text{tet}}$. This model is not consistent with
303 the omphacite model, even though the models overlap in composition space, and the two
304 should not be used in the same calculation. In particular, the simple M1 and M2 sites of
305 the augite model do not allow order-disorder to take place on either of these sites

306 individually, unlike the split M1 and M2 sites of the omphacite model. In partial
307 compensation for this, different values of ΔG^{mod} are used for some end-members that are
308 common to both models.

309 The heart of the augite model is the pyroxene quadrilateral
310 $\text{CaMgSi}_2\text{O}_6$ – $\text{Mg}_2\text{Si}_2\text{O}_6$ – $\text{Fe}_2\text{Si}_2\text{O}_6$ – $\text{CaFeSi}_2\text{O}_6$. Figure 1 shows the modelled fit to the
311 experimental work of Lindsley (1981, 1983) and Turnock & Lindsley (1981) on
312 clinopyroxene–orthopyroxene equilibria in this system, including the binary subsystem
313 $\text{CaFeSi}_2\text{O}_6$ – $\text{Fe}_2\text{Si}_2\text{O}_6$. The clinopyroxene a – x relations cover the whole of the quadrilateral
314 composition space, with the compositional end-members in appropriate $C2/c$ symmetry
315 being diopside (di), clinoenstatite (cenh), clinoferrosilite (cfs) and hedenbergite (hed). The
316 clinoenstatite and clinoferrosilite end-members are polymorphs that exist at low-pressure,
317 high-temperature in the unary systems, and their stability fields and properties are little
318 known. They are generated via ΔG^{tran} expressions from the $Pbca$ end-members en
319 (enstatite) and fs (ferrosilite) in the Holland & Powell dataset. An ordered intermediate
320 end-member, fmc ($\text{Mg}^{\text{M1}}\text{Fe}^{\text{M2}}\text{Si}_2\text{O}_6$), allows non-equal partitioning of $[\text{Mg}, \text{Fe}^{2+}]$ over the
321 M1 and M2 sites (Holland & Powell, 2006). Since a reaction $\text{di} + \frac{1}{2} \text{cfs} = \text{hed} + \frac{1}{2} \text{cenh}$ can
322 be written among the compositional end-members, the thermodynamic properties of one
323 must be treated as dependent, and hedenbergite was chosen for this purpose. Values for
324 model parameters on the $\text{CaMgSi}_2\text{O}_6$ – $\text{Mg}_2\text{Si}_2\text{O}_6$ join, including $\Delta G_{\text{cenh}}^{\text{tran}}$, were taken from the
325 CMAS clinopyroxene model of Green *et al.* (2012a), where they were calibrated against the
326 experimental work of Brey & Huth (1984); Carlson & Lindsley (1988); Lindsley & Dixon
327 (1976); Mori & Green (1975); Nickel & Brey (1984); Perkins & Newton (1980) and
328 Schweitzer (1982).

329 The MCTC function in THERMOCALC was used to fit the additional CFMS parameters
330 $W_{\text{di},[\text{cfs},\text{fmc}]}$, $W_{\text{cenh},[\text{cfs},\text{fmc}]}$, $W_{\text{cfs},\text{fmc}}$, $\Delta G_{\text{cfs}}^{\text{tran}}$ and $\Delta G_{\text{fmc}}^{\text{od}}$. The pressure dependence of the
331 inherited CMAS parameter $W_{\text{di},\text{cenh}}$ was applied to $W_{\text{di},[\text{cfs},\text{fmc}]}$. $\Delta G_{\text{cfs}}^{\text{tran}}$ was assumed to have
332 the same temperature dependence as $\Delta G_{\text{cenh}}^{\text{tran}}$, and was required to give a fs = cfs transition

333 curve consistent with the estimation of Lindsley (1981). $\Delta G_{\text{fmc}}^{\text{od}}$ took the mean pressure and
334 temperature dependencies of $\Delta G_{\text{cenh}}^{\text{tran}}$ and $\Delta G_{\text{cfs}}^{\text{tran}}$, with the constant term fitted such that
335 the ordered end-member fmc was more stable than its fully disordered equivalent,
336 $\text{Mg}_{\frac{1}{2}}^{\text{M1}}\text{Fe}_{\frac{1}{2}}^{\text{M1}}\text{Mg}_{\frac{1}{2}}^{\text{M2}}\text{Fe}_{\frac{1}{2}}^{\text{M2}}\text{Si}_2\text{O}_6$, for which G is given by $\frac{1}{2}(G_{\text{cenh}} + G_{\text{cfs}})$. At 900°C and 8 kbar,
337 the dependent value of G_{hed} was constrained to be within 2 kJ/mol of the ds62 dataset
338 value, with a further constraint of $G_{\text{hed}} < G_{\text{ohed}}$. G_{ohed} is the G function for the
339 *Pbca*-symmetry orthohedenbergite end-member, derived from the quadrilateral *a-x*
340 relations for orthopyroxene in the same way as G_{hed} is derived for the hedenbergite
341 end-member in clinopyroxene; thus the latter condition specified that the monoclinic
342 polymorph was the more stable of the two.

343 The resulting fit successfully reproduces augite–orthopyroxene tielines in the
344 quadrilateral, and is notably successful at matching the very sensitive divariant
345 augite–pigeonite–orthopyroxene equilibrium at 15 kbar, 1000°C (Fig. 1). It somewhat
346 overestimates the width of the augite–pigeonite solvus towards higher FeO/(FeO+MgO)
347 values.

348 The quadrilateral model was then combined with the CMAS clinopyroxene model of
349 Green *et al.* (2012a), introducing the end-member Ca-tschermak’s pyroxene (cats;
350 $\text{CaAl}_2\text{SiO}_6$) and associated parameters, which allowed for the substitution of Al onto the
351 M1 and tetrahedral sites simultaneously. The cats end-member exhibits internal
352 order-disorder of Si-Al on the tetrahedral site, with the energy and entropy of disordering
353 reduced by a factor of 4 (Holland & Powell, 2011). Finally, the end-members jadeite (jd)
354 and acmite (acm) were added to the model to accommodate Na, Fe^{3+} , and an excess of Al
355 on the M1 site relative to the tetrahedral site. Values for $W_{\text{di,jd}}$, $W_{\text{di,acm}}$ and $W_{\text{jd,acm}}$ were
356 adopted from the omphacite model. However, the jd and acm end-members serve a different
357 role in the augite model from in the omphacite model. In the augite model, they are simply
358 required to admit minor components, whereas in the omphacite model, they may be present
359 in substantial proportions, with order–disorder between sodic and calcic end-members

360 contributing heavily to the thermodynamics of mixing. Consequently it is not very
361 significant that the values of the dependent $W_{\text{hed},n}$ parameters in the augite model differ
362 from their independently-calibrated equivalents in the omphacite model (values are
363 compared in the Appendix). With the same justification a $\Delta G_{\text{jd}}^{\text{mod}}$ term was added to the
364 augite jd end-member, and different $\Delta G_{\text{acm}}^{\text{mod}}$ terms were used in the augite and omphacite
365 models.

366 In addition to $\Delta G_{\text{jd}}^{\text{mod}}$ and $\Delta G_{\text{acm}}^{\text{mod}}$, the free parameters in this second stage of augite
367 model calibration were $W_{\text{cats},[\text{cfs},\text{fmc}]}$, $W_{\text{jd},[\text{cenh},\text{cfs},\text{fmc},\text{cats}]}$ and $W_{\text{acm},[\text{cenh},\text{cfs},\text{fmc},\text{cats}]}$. These
368 interaction energies were not expected to be influential compared with the ΔG_i^{mod} terms, so
369 a small number of observed equilibria were carefully chosen to be fitted, primarily with the
370 purpose of finding values for $\Delta G_{\text{jd}}^{\text{mod}}$ and $\Delta G_{\text{acm}}^{\text{mod}}$. The chosen equilibria comprised two
371 natural rock samples, with estimated P and T values, and one experiment; Table 2 shows
372 the equilibria and results. The process of fitting with MCTC revealed very strong
373 multicomponent correlations among the interaction energies. It was not clear *a priori* that
374 these correlations would be relevant for model calculations in general, but in fact, in later
375 calculations on melting equilibria, it was found that violating the correlations for apparently
376 trivial parameters such as $W_{\text{cats},\text{fmc}}$ did indeed have a large and detrimental effect on the
377 calculated compositions of all phases, particularly the anorthite content x^{an} in plagioclase.

378 **Calculations with the augite versus omphacite models**

379 Figure 2 shows pseudosections calculated for an oxidised MORB composition, based on that
380 of Sun & McDonough (1989; SM89, Table 1), in the range 450–700°C and 4–20 kbar. The
381 figure is contoured for $x_{\text{Na}}^{\text{M2}}$ in clinopyroxene. Calculations were carried out with first the
382 augite model (Fig. 2a,b) and then the omphacite model (Fig. 2c,d), in order to compare the
383 two. The comparison demonstrates, firstly, that the omphacite model is the appropriate
384 choice for the relatively low temperatures shown. When modelling is done correctly using

385 the omphacite model (Fig. 2c,d), $x_{\text{Na}}^{\text{M2}}$ in clinopyroxene rises to > 0.4 towards higher
386 pressures, and the diopside–omphacite solvus is visible at several pressures with closure at
387 $\sim 600^\circ\text{C}$. Meanwhile the augite model has no capacity to model omphacite-like Na contents
388 or coexistence between omphacitic and diopsidic compositions, so no solvus appears in Figs
389 2a and b. Secondly, it can be seen that the two models give substantially consistent results
390 for $P < 13$ kbar and $T > 600^\circ\text{C}$, where the omphacite model takes on an augitic
391 composition. Phase field boundaries in this region in Figs 2a and c show agreement within
392 20°C , while the augite model gives values of $x_{\text{Na}}^{\text{M2}}$ that are consistently lower than the
393 omphacite model by ~ 0.05 , within the likely uncertainty in the modelling.

394 The nature of phase relations in Fig. 2c are discussed in a later section. Subsequent
395 figures will demonstrate the behaviour of the augite model in the $P < 13$ kbar, $T > 600^\circ\text{C}$
396 regime for which it was calibrated.

397 CLINOAMPHIBOLE *A*–*X* RELATIONS

398 The clinoamphibole model of Diener *et al.* (2007) and Diener & Powell (2012), in
399 NCFMASHO, is suitable for calculations on metabasic rocks under subsolidus conditions,
400 using version 5.5 of the dataset (Holland & Powell, 1998). As described above, it was
401 updated for use with version 6.2 in conjunction with the omphacite model, by adjustments
402 to the end-member thermodynamics. The resulting modifications affected the following
403 end-members: pargasite ($\Delta G_{\text{parg}}^{\text{mod}}$ changed from 15 kJ to -10 kJ), glaucophane ($\Delta G_{\text{gl}}^{\text{mod}}$
404 changed from 3 kJ to -3 kJ), cummingtonite ($\Delta G_{\text{cumm}}^{\text{mod}}$ changed from -6.4 kJ to 0 kJ),
405 grunerite ($\Delta G_{\text{grun}}^{\text{mod}}$ changed from -5 kJ to -3 kJ) and magnesioriebekite ($\Delta G_{\text{mrb}}^{\text{make}}$ changed
406 from 8 kJ to 0 kJ). These were pleasing in that generally the absolute values of the $\Delta G_{\text{i}}^{\text{mod}}$
407 terms decreased, making the end-member *G* curves more similar to the dataset functions.

408 By granulite facies temperatures, the components K_2O and TiO_2 are significant in
 409 hornblende (e.g. Robinson *et al.*, 1982). The core model was therefore expanded to include
 410 the components K_2O and TiO_2 , with the intention that the full model in NCKFMASHTO
 411 would be applicable both above and below the solidus. K_2O was introduced via a
 412 potassium-pargasite end-member (kprg, $KCa_2Mg_4Al_3Si_6O_{22}(OH)_2$), such that K^+ mixes
 413 with Na^+ on the partially filled model A site. A deprotonation-style substitution was
 414 adopted to introduce TiO_2 via an end-member Ti-tschermakite (tts, $Ca_2Mg_3Ti_2Al_2Si_6O_{22}$),
 415 allowing hornblende to persist to higher temperatures in equilibrium with melt by lowering
 416 its water activity $a(H_2O)$, although in reality the substitution whereby TiO_2 enters
 417 metamorphic hornblende is more likely to be a tschermakite-like and/or glaucophane-like
 418 substitution (Schumacher, 2007). The new end-members tts and kprg are not present in the
 419 Holland & Powell dataset, but are made via the reactions $kprg = mu - pa + parg +$
 420 ΔG_{kprg}^{make} and $tts = dsp - 2 ru + ts + \Delta G_{tts}^{make}$ (mu: muscovite; pa: paragonite; ru: rutile;
 421 dsp: diaspore).

422 A key equilibrium is the first introduction of hornblende and glaucophane to the
 423 assemblage $act + chl + ep + ab + sph + q + H_2O \pm bi$, i.e. the junction of the greenschist,
 424 blueschist and amphibolite facies. This occurs at around 8–10 kbar and 450–500°C on most
 425 metamorphic facies diagrams. The presence of three coexisting amphiboles in this
 426 equilibrium make the calculated values of P , T and compositional variables extremely
 427 sensitive to the parameterisation of the amphibole $a-x$ relations. It was required that
 428 minimal amounts of K_2O and TiO_2 should be taken into the amphiboles at this
 429 temperature, but the prejudice was nevertheless imposed that the amphibole phases would
 430 incorporate K_2O in the order $hb > gl \approx act$, and TiO_2 in the order $hb \approx gl > act$. The full
 431 list of $P-T$ and compositional constraints placed on this equilibrium during fitting, and the
 432 results obtained, are given in Table 3. The table also compares calculations and
 433 observations for several upper-amphibolite facies rocks, for which likely values of P , T and
 434 M_O have been established by previous calculations with older versions of the models. Since

435 some of these equilibria contain clinopyroxene, this was also an opportunity to check the
436 behaviour of the ds6-omphacite and augite models.

437 Fitting was carried out in MCTC, to find values for $\Delta G_{\text{kprg}}^{\text{make}}$, $\Delta G_{\text{tts}}^{\text{make}}$, and the new
438 interaction energies $W_{\text{kprg},n}$ and $W_{\text{tts},n}$. Because the number of interaction energies to be
439 fitted was large, and they were expected to be poorly constrained due to the small amounts
440 of the K_2O and TiO_2 end-members present, the fitting problem was initially reduced by
441 assuming that K^+ and Na^+ would mix with similar energetic consequences on the A-site,
442 and therefore fixing values of $W_{\text{parg,kprg}} = 0$ and $W_{\text{kprg},n} = W_{\text{parg},n}$. The possibility of
443 allowing other, less well constrained parameters to vary in order to improve the fit was also
444 explored. Ultimately however, better results were obtained by allowing the $W_{\text{kprg},n}$
445 parameters to diverge from the equivalent $W_{\text{parg},n}$ values by up to 5 kJ, while the
446 parameters from the core NCFMASHO model could not convincingly be improved upon.
447 The asymmetry of interactions was inherited from the Diener *et al.* (2007) model, with the
448 addition of the terms $\alpha_{\text{kprg}} = \alpha_{\text{parg}}$ and $\alpha_{\text{tts}} = \alpha_{\text{ts}}$. As in the Diener *et al.* (2007) model and
449 the new augite model, the entropy of Si–Al mixing on the tetrahedral sites was reduced by a
450 factor of 4.

451 CALCULATIONS ON SUBSOLIDUS PHASE RELATIONS

452 We now return to Fig. 2c, a pseudosection calculated between greenschist–blueschist facies
453 conditions and the solidus using the metabasite set of a – x relations, with the omphacite
454 model representing clinopyroxene. The bulk composition (SM89, Table 1) is based on the
455 MORB composition of Sun & McDonough (1989), but considerably oxidised, with $X_{\text{Fe}^{3+}} =$
456 $\text{Fe}^{3+}/(\text{Fe}^{2+} + \text{Fe}^{3+}) = 0.36$. The same bulk composition was previously used by Diener &
457 Powell (2012), fig. 1c, allowing the ds55 and ds6x generations of a – x relations to be

458 compared.

459 Subsolidus phase relations in the greenschist and amphibolite facies remain similar, with
460 hornblende replacing actinolite and chlorite at $\sim 480^\circ\text{C}$ as in the older calculations, and
461 diopside now joining the assemblage at $\sim 550^\circ\text{C}$ rather than 600°C . Calculations at 12–20
462 kbar and $< 550^\circ\text{C}$ now generate $\text{gl} + \text{act} + \text{chl} + \text{ep} \pm \text{law} \pm \text{o}$ assemblages that resemble
463 natural blueschists, whereas the ds55 generation of a - x relations found omphacite stable
464 rather than glaucophane. At 16–20 kbar, between 530 and 580°C , the blueschist
465 assemblages give way to higher-temperature eclogite assemblages containing garnet,
466 omphacite and hornblende.

467 Phase relations below 650°C are negligibly affected if the K_2O and TiO_2 components
468 are excluded from amphibole. The Diener & Powell (2012) figure was calculated without a
469 melt phase, since no suitable melt a - x relations existed at that time; the new figure, using
470 the metabasite melt model described in the next section, shows the start of H_2O -saturated
471 melting at 615 – 700°C .

472 MELT A - X RELATIONS

473 Existing silicate melt a - x relations for use with the Holland & Powell dataset include the
474 ds5 haplogranitic model of Holland & Powell (2001), its expansion into NCKFMASH for
475 use in metapelite melting calculations (White *et al.*, 2001, 2007), the ds6 equivalent of the
476 metapelite melt model (White *et al.*, 2014), and the mafic melt model of Jennings &
477 Holland (2015). These models are exceedingly simple, reproducing the macroscopic mixing
478 properties of melt over a limited compositional range while making no attempt to capture
479 melt speciation, or otherwise to separate the enthalpic and entropic contributions in the
480 models in a way that resembles reality. Like the a - x relations for solid solutions, the melt is

481 treated as a regular solution with the non-ideal enthalpy of mixing expressed using the
482 symmetric formalism. The end-members are mineral-like compounds that mix as molecules.

483 The metabasite melt model has proved very successful in calculations (e.g. White *et al.*,
484 2001, 2007; Grant, 2009; Johnson *et al.*, 2008; White *et al.*, 2011). It is desirable that the
485 new metabasite melt model and the metapelite melt model should share a core in NKASH,
486 defined by the end-members $qL-abL-kspL-h2oL$ (see Appendix for end-member
487 definitions). However, with respect to the CaO, FeO and MgO components, the metabasite
488 melt model requires a different parameterisation and structure from the metapelite model,
489 in order to allow the melt composition to become sufficiently calcic, and to become
490 metaluminous if required.

491 The $qL-abL-kspL$ subsystem of the White *et al.* (2014) metapelite melt model was
492 strongly constrained by the experiments of Boyd & England (1963); Lindsley (1966);
493 Ostrovsky (1966) and Jackson (1976), and could be retained without change to form the
494 core of the metabasite melt model. In the $qL-abL-kspL-h2oL$ subsystem, a number of
495 changes are planned for a forthcoming revision of the White *et al.* (2014) metapelite melt
496 model, and these have been incorporated directly into the metabasite melt model as
497 presented in this study. The changes to the $qL-abL-kspL-h2oL$ core, relative to the White
498 *et al.* (2014) version of the metapelite melt model, are as follows. (1) The interaction
499 energies $W_{h2oL,[qL,abL,kspL]}$ have been refined by comparison with the subsystem experiments
500 of Behrens (1995); Kennedy *et al.* (1962); Stewart (1967); Goldsmith & Peterson (1990) and
501 Goldsmith & Jenkins (1985). (2) In ds63, the constant-pressure heat capacity of the h2oL
502 end-member has been lowered to improve the calculated H₂O isopleths for melts. In fig. 9 of
503 Holland & Powell (2001) the H₂O isopleths in granitic liquid are spuriously concave
504 downwards in pressure, as a result of too high a heat capacity for h2oL; this heat capacity
505 has now been optimised such that the isopleths become approximately straight lines, as
506 required by the experimental data of Holtz *et al.* (1995). (3) The formula of the
507 end-member silL has been changed from $\frac{8}{5}Al_2SiO_5$ to Al_2SiO_5 .

508 In the metapelite model, the Ca-rich vertex of composition space is represented by the
509 anorthite-liquid end-member, anL, but the metabasite model has been extended as far as a
510 wollastonite-liquid end-member, woL, in order to encompass metaluminous compositions.
511 However, the woL end-member is compositionally distant from the melts of metabasic
512 rocks, and its thermodynamics are poorly constrained. To compensate for this, an
513 anL-composition end-member was restored to the metabasite melt model in the form of an
514 ordered intermediate, made via the reaction $\text{anL} = \text{woL} + \text{silL}$ with a $\Delta G_{\text{anL}}^{\text{od}}$ term applied.
515 The thermodynamic properties of $\text{CaAl}_2\text{Si}_2\text{O}_8$ -composition liquid were approximated by
516 fitting to the anorthite melting curve. This aspect of the model structure follows e.g. Hastie
517 (1983); Hastie & Bonnell (1985); Bonnell & Hastie (1985); Besmann & Spear (2002) and
518 Green *et al.* (2012b), in which the ordered intermediate end-members are termed ‘associate
519 species’. The inclusion of an ordered intermediate end-member, intL, in the melt $a-x$
520 relations adds flexibility in fitting the available constraints, since the $\Delta G_{\text{intL}}^{\text{od}}$ term provides a
521 free parameter and the presence of the intL compound contributes to model entropy.
522 However it should be stressed that speciation is not represented in any meaningful way in
523 the metabasite melt model, either by the choice of end-member mixing units or by the
524 ordering taking place among them.

525 To complete the calibration of the metabasite melt model, values had to be found for
526 $\Delta G_{\text{anL}}^{\text{od}}$ and the new interaction energies $W_{\text{woL},nL}$ and $W_{\text{anL},nL}$. Parameters such as $W_{\text{anL},qL}$
527 are not strictly the same as the equivalently-named parameter in the metapelite melt
528 model, because the anL end-member in the metabasite melt model is not the dataset
529 end-member but an ‘ordered’ end-member that coexists with a 1:1 mixture of woL + silL
530 ‘molecules’, even at the anorthite composition. Due to the significant difference in
531 composition range between the metapelite and metabasite melt models, the non-core
532 parameters from the metapelite melt model were considered to be potentially subject to
533 variation in MCTC, namely the interaction energies $W_{[\text{silL},\text{foL},\text{faL}],nL}$ and the $\Delta G_{[\text{silL},\text{foL},\text{faL}]}^{\text{mod}}$. A
534 finite $\Delta G_{\text{woL}}^{\text{mod}}$ was also explored.

535 Calibration in MCTC was carried out simultaneously on (a) the wet and dry melting
536 curves of anorthite (the experiments of Goldsmith (1980); Yoder (1976) and Stewart (1967),
537 constraining the woL–silL and woL–silL–h2oL compositional joins of the melt model), (b)
538 the inferred position of the hb + di + opx + an + q + L + H₂O invariant point in the
539 CMASH system, from Ellis & Thompson (1986), (c) two reported melt compositions at
540 large melt fraction, from the TTG-genesis studies of Patiño Douce & Beard (1995, SQA
541 composition) and Beard & Lofgren (1991, Sample 478), and (d) nine estimates of phase
542 boundary positions (H₂O-out, orthopyroxene-out, hornblende-out, melt-out, quartz-out,
543 plagioclase-out) in the same two experimental bulk compositions. The studies of Patiño
544 Douce & Beard (1995) and Beard & Lofgren (1991) were chosen because the experiments
545 represent a comprehensive P – T grid for $P \leq 12.5$ kbar. The results of the calibration are
546 shown below.

547 **CALCULATIONS ON EXPERIMENTAL COMPOSITIONS**

548 Figures 3 and 4 present pseudosections calculated for hydrate-breakdown melting using bulk
549 compositions SQA (Patiño Douce & Beard, 1995) and Sample 478 (Beard & Lofgren, 1991,
550 hereafter BL478). Bulk composition is treated as constant for experiments on one starting
551 material in one type of apparatus.

552 **Experiments of Patiño Douce & Beard (1995)**

553 The experiments of Patiño Douce & Beard (1995) on SQA, a synthetic quartz amphibolite,
554 yielded assemblages of q + pl + ilm/ru ± hb ± opx ± g ± cpx. Experiments at > 6 kbar
555 were performed in a piston cylinder and experiments at < 6 kbar in an internally heated
556 pressure vessel (IHPV). In Fig. 3a, calculations at > 6 kbar used a value of M_O that gave

557 $X_{\text{Fe}^{3+}} = 0.1$, while calculations < 6 kbar took place with $X_{\text{Fe}^{3+}} = 0.25$. These values reflect
558 the more oxidising environment of the IHPV relative to the piston cylinder, and were
559 chosen because they span a range of $X_{\text{Fe}^{3+}}$ values inferred from modelling of natural
560 amphibolites and granulites (see Table 1), although they may not correspond closely to the
561 unknown $X_{\text{Fe}^{3+}}$ values developed in the experimental apparatus. For each of the two bulk
562 compositions, calculated values of fO_2 fall within the ranges estimated in the experiments,
563 but this does not sensitively constrain appropriate values for M_O . A single estimate for
564 $M_{\text{H}_2\text{O}}$ was applied to both high- and low-pressure calculations, obtained by Patiño Douce &
565 Beard (1995) through electron probe analysis of the melted starting mixture. In reality, the
566 starting material likely underwent substantial reduction or oxidation in each of the two
567 assemblies, mediated by infiltration or loss of hydrogen and associated with changes in M_O
568 and $M_{\text{H}_2\text{O}}$. However, we did not attempt to simulate the relationship between $M_{\text{H}_2\text{O}}$ in the
569 high-pressure, low- M_O experiments versus the low-pressure, high- M_O experiments, given
570 that the initial value of $X_{\text{Fe}^{3+}}$ in the starting material is unknown.

571 The calculations successfully reproduce the major assemblage changes of the
572 amphibolite–granulite transition as characterised by the experiments, specifically through
573 the up-temperature appearance of orthopyroxene and exhaustion of hornblende
574 (summarised in Fig. 3b). The hornblende-out boundary is well defined by the experiments,
575 and the calculations match this constraint reasonably well, although they predict a
576 shallower dP/dT slope for the boundary than the experiments suggest. For the chosen
577 values of M_O and $M_{\text{H}_2\text{O}}$, the calculations progressively underestimate the temperature of
578 hornblende exhaustion towards lower pressure. Garnet appears up to 0.6 kbar below the
579 minimum pressure permitted by the experiments, and at the highest pressures the
580 orthopyroxene-in boundary moves rapidly towards excessive temperatures. In the
581 experiments at 840°C and at 875°C, 10 kbar, the experimental assemblage is hb + pl + q +
582 Fe-Ti oxides, while the calculations additionally contain aug + L ± opx ± g. The
583 experimental assemblage is unchanged from that of the starting materials, so an approach

584 to the stable equilibrium assemblage cannot be demonstrated. Despite the moderate
585 temperatures and very long run durations of 1–2 weeks, the shortage of vapour or a
586 detectable volume of melt may inhibit equilibration, and it is likely that stable assemblages
587 at these conditions do indeed include clinopyroxene \pm orthopyroxene \pm melt.

588 Figure 3c shows the effect of oxidation state on the calculated assemblages at $P = 7$
589 kbar, over a range of $0 < M_{\text{O}} < 1.62$ mole% ($0 < X_{\text{Fe}^{3+}} < 0.50$). Under the relatively
590 reduced conditions assumed for the piston cylinder assembly, the temperature of the
591 hornblende-out boundary in particular is a strong function of M_{O} , rising from 830°C to
592 905°C over the range $0 < M_{\text{O}} < 0.5$ mole% ($0 < X_{\text{Fe}^{3+}} < 0.15$), although further increase in
593 M_{O} to 1.62 mole% raises the hornblende-out temperature by only 40°C. The sensitivity of
594 the boundary under low- M_{O} conditions demonstrates the difficulties of extracting
595 calibration information from even the best devised and most careful experimental study,
596 and also highlights the sensitivity of future forward-modelling results to the assumed bulk
597 O content. This sensitivity should always be quantitatively investigated via T – M_{O} and
598 P – M_{O} plots (e.g. White *et al.*, 2000; Diener & Powell, 2010; Korhonen *et al.*, 2012).

599 The equivalent analysis for $M_{\text{H}_2\text{O}}$ at 7 kbar is shown in Fig. 3d. At $M_{\text{H}_2\text{O}} = 4.6$ mol%,
600 the value used in Fig. 3a, the calculations predict a H_2O -present solidus at 665°C, leading
601 to a volumetric melt fraction of 0.33 at 900°C (Fig. 3e). By contrast, the experiments are
602 thought to represent hydrate-breakdown melting and produce only modest melt fractions at
603 900°C. However, by reducing the estimate of $M_{\text{H}_2\text{O}}$ in Fig. 3a from 4.6 mole% to 3.0 mole%,
604 a fluid-absent solidus could be calculated at 800°C without significantly degrading the fit to
605 the experimental hornblende-out boundary, the latter being only a weak function of $M_{\text{H}_2\text{O}}$.
606 A value of $M_{\text{H}_2\text{O}} = 3.0$ mole% is in fact close to the estimate of bulk H_2O in the starting
607 materials based on mineral modes ($M_{\text{H}_2\text{O}} \sim 3.3$ mole%, Patiño Douce & Beard, 1995). For
608 a boundary as sensitive to bulk H_2O as the water-undersaturated solidus, it is difficult to
609 make a meaningful comparison between calculations and observations, given that the
610 appropriate value of bulk H_2O in the experimental run products is poorly known.

611 **Experiments of Beard & Lofgren (1991)**

612 Sample 478 from the study of Beard & Lofgren (1991; BL478) is a naturally occurring
613 low-K₂O andesite, less siliceous and less potassic than the SQA material of Patiño Douce &
614 Beard (1995) and with higher bulk FeO/(FeO+MgO). Hydrate-breakdown melting
615 experiments, conducted in an IHPV, produced assemblages of pl + melt + Fe-Ti oxides ±
616 cpx ± opx ± hb ± q, as shown in Fig. 4a.

617 Calculations on this bulk composition again describe an amphibolite to granulite facies
618 transition that is broadly consistent with the experiments, summarised in Fig. 4b. As for
619 the SQA composition, the calculated prediction of clinopyroxene stability conflicts with the
620 lowest-temperature experiment at 850°C, 6.9 kbar. This experiment yielded pargasitic
621 amphibole + q + pl + Fe-Ti oxides + 6.2 wt% L, whereas the starting assemblage was
622 actinolitic amphibole + q + pl + Fe-Ti oxides. We tentatively suggest that the small
623 quantity of melt present in an otherwise dry experiment may again have been insufficient to
624 allow the stable crystalline assemblage to form. If this is the case, the experiments again
625 primarily define an upper temperature limit on the hornblende-out boundary. The
626 calculated quartz-out boundary lies at too high a temperature, but is shown in Fig. 4c and
627 d to be particularly sensitive to M_{O} and $M_{\text{H}_2\text{O}}$. At 900°C and 1 kbar the calculations
628 predict H₂O as a free phase, so they are compared with the results of an H₂O-saturated
629 experiment on the same starting material, but fail to reproduce the observed amphibole +
630 quartz assemblage. This is not a significant concern, as the focus of the model calibration
631 was on the more geologically relevant situation of hydrate-breakdown melting (Brown &
632 Fyfe, 1970).

633 The value of M_{O} chosen for the calculations in Fig. 4a corresponds to $X_{\text{Fe}^{3+}} = 0.2$, which
634 was assumed to be plausible for the natural starting material, and consistent with exposure
635 to the IHPV assembly over moderate run durations of around 90–120 hours. The T – M_{O}
636 plot (Fig. 4c) shows that, for the relatively oxidised conditions imposed, the calculated 7

637 kbar position of the hornblende-out boundary varies only from 885°C at $M_{\text{O}} = 0.76$ mole%
638 ($X_{\text{Fe}^{3+}} = 0.15$) to 902°C at $M_{\text{O}} = 1.27$ mole% ($X_{\text{Fe}^{3+}} = 0.25$). The hornblende-out boundary
639 is also almost indifferent to $M_{\text{H}_2\text{O}}$ in the range 0.5 to 4.5 mole% (Fig. 4d). The value of
640 $M_{\text{H}_2\text{O}}$ chosen for Fig. 4a is 3.42 mole%, larger than the 1.72 mole% estimated by loss on
641 ignition from the starting materials by Beard & Lofgren (1991). In our modelling, this
642 choice of $M_{\text{H}_2\text{O}}$ leads to the coexistence of orthopyroxene and hornblende over a narrow
643 ($\sim 50^\circ\text{C}$) temperature range, whereas for values of $M_{\text{H}_2\text{O}} < 3.1$ mole%, orthopyroxene joins
644 the assemblage at rather low temperatures and creates a wide field of hornblende-granulite.

645 **Hornblende-out boundaries in various experimental studies**

646 Since only two bulk compositions from TTG-genesis experiments were used in the model
647 calibration, Fig. 5 summarises the results of calculations on the hornblende-out boundary in
648 four additional bulk compositions that were not involved in the calibration process, taken
649 from the hydrate-breakdown melting studies of Beard & Lofgren (1991); Rushmer (1991);
650 Wolf & Wyllie (1994) and Skjerlie & Patiño Douce (1995). Comparable calculations for
651 SQA and BL478, the compositions used in calibration, are also shown. In each case, the
652 true temperature of the hornblende-out boundary could be inferred with some confidence
653 from an isobaric sequence of experiments, in which the final hornblende coexisted with a
654 moderate melt fraction and had an apparently equilibrated composition. The calculations,
655 shown as blue bars, locate the hornblende-out boundary for each experimental phase
656 assemblage. Where possible, calculations were performed over generous ranges of $M_{\text{H}_2\text{O}}$
657 (3.5–6.5 mole%, equivalent to ~ 1 –2 wt%) and M_{O} (such that $0.1 < X_{\text{Fe}^{3+}} < 0.25$), varied
658 simultaneously, which we expect to encompass the true experimental values in most cases.
659 For bulk compositions WW94 and BL571, the experimental assemblage could only be
660 calculated over a reduced range of M_{O} or $M_{\text{H}_2\text{O}}$; see Fig. 5 and Table 1.

661 The calculations generally reproduce the experimental hornblende-out temperatures

662 well, although they considerably overestimate the temperature for the IAT (island arc
663 tholeiite) composition of Rushmer (1991). Temperatures are probably underestimated for
664 the natural amphibolite composition AGS11.1 of Skjerlie & Patiño Douce (1995), and the
665 calibration composition SQA. Over- or under-estimation of hornblende-out temperature
666 may be correlated with molar bulk values of $\text{Al}_2\text{O}_3/(\text{CaO} + \text{Na}_2\text{O} + \text{K}_2\text{O})$, of which IAT
667 has the highest value and AGS11.1 and SQA relatively low values.

668 To a considerable extent the variation of modelled boundaries with bulk composition is
669 a function of the well established Holland & Powell (2011) dataset calibration, combined
670 with the superimposed ΔG_i^{mod} and ΔG_i^{make} terms. Therefore it is perhaps unsurprising that
671 the results of these calculations are reasonable, even though only two of the TTG-genesis
672 studies were incorporated into the fitting.

673 DISCUSSION

674 The newly calibrated $a-x$ relations extend the scope of phase-equilibrium forward-modelling
675 methods to include metabasic rocks at high temperature. A pseudosection approach to
676 thermobarometry is now feasible for such rocks, and other questions that incorporate a bulk
677 composition constraint, such as limits on melt loss, may now be addressed. Methods of this
678 kind have previously brought insight into metamorphic processes in metapelites (e.g. White
679 *et al.*, 2003; Kelsey *et al.*, 2003; Johnson & Brown, 2004; Halpin *et al.*, 2007; Streule *et al.*,
680 2010; Korhonen *et al.*, 2010; Palin *et al.*, 2012). Strictly the calibration of the $a-x$ relations
681 described in this paper was limited to ≤ 13 kbar, owing to the lack of a thermodynamic
682 model for aqueous fluid containing dissolved silicate material. However, it is reasonable to
683 use the metabasite models with caution whenever the results can be compared with
684 observations to demonstrate that appropriate stable assemblages are calculated. In the

685 companion paper, Palin *et al.* (2016b), we examine calculations with the metabasite models
686 on a variety of natural compositions, comparing the calculated assemblages and melt
687 compositions with expectations drawn from observation and experiment.

688 Through the above comparison of phase diagram calculations with experiments, it is
689 possible to comment on the uncertainties and limitations of the models. The models can
690 probably be expected to give a correct sequence of up-temperature assemblages, with
691 respect to major phases. Within the calibration range of the a - x relations,
692 phase-in/phase-out boundaries are likely to be constrained to within 50–100°C, or 1–2 kbar
693 for a strongly pressure-dependent boundary, allowing for the difficulty of assessing M_{O} and
694 $M_{\text{H}_2\text{O}}$ during model calibration. Comparable magnitudes of uncertainty are associated with
695 estimating a representative bulk composition for an equilibrium assemblage in a natural
696 rock sample (Palin *et al.*, 2016a). As in all forward modelling of phase equilibria, careful
697 consideration of the sensitivity of results to M_{O} and $M_{\text{H}_2\text{O}}$ will be essential for meaningful
698 interpretation.

699 As metabasic rocks typically contain fewer phases than metapelites, fields on P - T
700 pseudosections tend to be larger, providing a less useful constraint on the pressure and
701 temperature of mineral preservation. It may therefore be desirable to estimate P - T more
702 precisely by comparing the observed and calculated compositions of phases. An appropriate
703 way to do this, that correctly takes account of the uncertainties in the thermodynamic
704 modelling, is the ‘average P - T ’ method of Powell & Holland (1988) and Powell & Holland
705 (1994). This can be carried out in THERMOCALC, using the standard input files for the
706 Holland & Powell (2011) dataset and metabasite set of a - x relations, just as for
707 pseudosection calculations (Powell & Holland, 2008). The average P - T method finds the
708 least-squares best estimate of P -at- T or T -at- P using the thermobarometric information
709 contained in multiple independent reactions among model end-members. Starting from the
710 activities calculated for the model end-members at the analytical phase compositions, it
711 makes minimal uncertainty-weighted adjustments to the activities and enthalpies of the

712 end-members, until the constraint is satisfied that all end-member reactions must meet at
713 an equilibrium P or T (both P and T can be constrained using the uncertainty output).
714 When good statistical diagnostics are obtained from the procedure, they suggest both that
715 the analysed phases are well equilibrated, and that the thermodynamic models are
716 sufficiently well calibrated to reflect this.

717 The $a-x$ relations presented in this paper should be considered only as a starting point
718 for the modelling of high-temperature metabasic assemblages. Future $a-x$ development is
719 expected to include a single model for clinopyroxene, replacing the current omphacite and
720 augite models, and a single model for tonalitic–trondjhemitic to granitic melt, replacing the
721 current metabasite and metapelite melt models. The set of metabasite $a-x$ models will be
722 refined over time, as was the metapelite set of models before it, to correct systematic
723 problems that emerge in calculated phase equilibria. We welcome feedback from users on
724 the performance of the models.

725 **ACKNOWLEDGEMENTS**

726 We are grateful to Sebastian Fischer for his labours in compiling an experimental database,
727 and to Luca Ziberna for illuminating discussions about experimental methods. We thank
728 Katy Evans, David M. Jenkins and Gary Stevens for their insightful and constructive
729 reviews, and Mike Brown for his editorial handling. This work was supported by DFG grant
730 WH 110/4-1 awarded to R. W. White.

731 **REFERENCES**

- 732 Adam, J., Green, T. H. & Day, R. A., 1992. An experimental study of two garnet
733 pyroxenite xenoliths from the Bullenmerri and Gnotuk Maars of western Victoria,
734 Australia. *Contributions to Mineralogy and Petrology*, **111**, 505–514.
- 735 Asimow, P. D., Dixon, J. E. & Langmuir, C. H., 2004. A hydrous melting and fractionation
736 model for mid-ocean ridge basalts: application to the Mid-Atlantic Ridge near the
737 Azores. *Geochemistry, Geophysics, Geosystems*, **5**, Q01E16.
- 738 Auzanneau, E., Vielzeuf, D. & Schmidt, M. W., 2006. Experimental evidence of
739 decompression melting during exhumation of subducted continental crust. *Contributions*
740 *to Mineralogy and Petrology*, **152**, 125–148.
- 741 Beard, J. S. & Lofgren, G. E., 1991. Dehydration melting and water-saturated melting of
742 basaltic and andesitic greenstones and amphibolites. *Journal of Petrology*, **32**, 365–401.
- 743 Behrens, H., 1995. Determination of water solubilities in high-viscosity melts: an
744 experimental study on NaAlSi₃O₈ melts. *European Journal of Mineralogy*, **7**, 905–920.
- 745 Berman, R. G., 1988. Internally-consistent thermodynamic data for minerals in the system
746 Na₂O–K₂O–CaO–MgO–FeO–Fe₂O₃–Al₂O₃–SiO₂–TiO₂–H₂O–CO₂. *Journal of*
747 *Petrology*, **29**, 445–522.
- 748 Besmann, T. M. & Spear, K. E., 2002. Thermochemical modeling of oxide glasses. *Journal*
749 *of the American Ceramic Society*, **85**, 2887–2894.
- 750 Bonnell, D. W. & Hastie, J. W., 1985. A predictive thermodynamic model for complex
751 high-temperature solution phases II. *High Temperature Science*, **26**, 313–334.
- 752 Boyd, F. R. & England, J. L., 1963. The effect of pressure on the melting of diopside,
753 CaMgSi₂O₆, and albite, NaAlSi₃O₈, in the range up to 50 kilobars. *Journal of*
754 *Geophysical Research*, **68**, 311–323.

- 755 Brey, G. & Huth, J., 1984. The enstatite–diopside solvus to 60 kbar. *Proceedings of the*
756 *Third International Kimberlite Conference*, **2**, 257–264.
- 757 Brooker, R., Holloway, J. R. & Hervig, R., 1998. Reduction in piston-cylinder experiments:
758 the detection of carbon infiltration into platinum capsules. *American*
759 *Mineralogist*, **83**, 985–994.
- 760 Brown, G. C. & Fyfe, W. S., 1970. The production of granitic melts during
761 ultrametamorphism. *Contributions to Mineralogy and Petrology*, **28**, 310–318.
- 762 Carlson, W. P. & Lindsley, D. H., 1988. Thermochemistry of pyroxenes on the join
763 $\text{Mg}_2\text{Si}_2\text{O}_6$ – $\text{CaMgSi}_2\text{O}_6$. *American Mineralogist*, **73**, 242–252.
- 764 Chatterjee, N. D., Krüger, R., Haller, G. & Olbricht, W., 1998. The Bayesian approach to
765 an internally consistent thermodynamic database: theory, database, and generation of
766 phase diagrams. *Contributions to Mineralogy and Petrology*, **133**, 149–168.
- 767 Chu, X. & Ague, J. J., 2013. Phase equilibria for graphitic metapelite including solution of
768 CO_2 in melt and cordierite: implications for dehydration, partial melting and graphite
769 precipitation. *Journal of Metamorphic Geology*, **31**, 843–862.
- 770 Coggon, R. & Holland, T. J. B., 2002. Mixing properties of phengitic micas and revised
771 garnet–phengite thermobarometers. *Journal of Metamorphic Geology*, **20**, 683–696.
- 772 De Paoli, M. C., 2006. *Cretaceous high-P granulite and high-T eclogite metamorphism at*
773 *Breaksea Sound, SW New Zealand*. PhD thesis, University of Sydney School of
774 Geosciences.
- 775 Diener, J. F. A. & Powell, R., 2010. Influence of ferric iron on the stability of mineral
776 assemblages. *Journal of Metamorphic Geology*, **28**, 599–613.
- 777 Diener, J. F. A. & Powell, R., 2012. Revised activity–composition models for clinopyroxene
778 and amphibole. *Journal of Metamorphic Geology*, **30**, 131–142.

- 779 Diener, J. F. A., Powell, R., White, R. W. & Holland, T. J. B., 2007. A new thermodynamic
780 model for clino- and orthoamphiboles in $\text{Na}_2\text{O}-\text{CaO}-\text{FeO}-\text{MgO}-\text{Al}_2\text{O}_3-\text{SiO}_2-\text{H}_2\text{O}-\text{O}$.
781 *Journal of Metamorphic Geology*, **25**, 631–656.
- 782 Dolejš, D. & Manning, C. E., 2010. Thermodynamic model for mineral solubility in aqueous
783 fluids: theory, calibration and application to model fluid-flow systems.
784 *Geofluids*, **10**, 20–40.
- 785 Droop, G. T. R., 1987. A general equation for estimating Fe^{3+} concentrations in
786 ferromagnesian silicates and oxides from microprobe analyses, using stoichiometric
787 criteria. *Mineralogical Magazine*, **51**, 431–435.
- 788 Ellis, D. J. & Thompson, A. B., 1986. Subsolidus and partial melting reactions in the
789 quartz-excess $\text{CaO} + \text{MgO} + \text{Al}_2\text{O}_3 + \text{SiO}_2 + \text{H}_2\text{O}$ system under water-excess and
790 water-deficient conditions to 10 kb: some implications for the origin of peraluminous
791 melts from mafic rocks. *Journal of Petrology*, **27**, 91–121.
- 792 Foley, S. F., Buhre, S. & Jacob, D. E., 2003. Evolution of the Archaean crust by
793 delamination and shallow subduction. *Nature*, **421**, 249–252.
- 794 Gerya, T. V., Maresch, W. V., Burchard, M., Zakhartchouk, V., Doltsinis, N. L. &
795 Fockenberg, T., 2005. Thermodynamic modeling of solubility and speciation of silica in
796 $\text{H}_2\text{O}-\text{SiO}_2$ fluid up to 1300°C and 20 kbar based on the chain reaction formalism.
797 *European Journal of Mineralogy*, **17**, 269–283.
- 798 Ghiorso, M. S. & Sack, R. O., 1995. Chemical mass transfer in magmatic processes, IV, a
799 revised and internally consistent thermodynamic model for the interpolation and
800 extrapolation of liquid-solid equilibria in magmatic systems at elevated temperatures and
801 pressures. *Contributions to Mineralogy and Petrology*, **119**, 197–212.
- 802 Ghiorso, M. S., Hirschmann, M. M., Reiners, P. W. & Kress, V. C., 2002. The pMELTS: A
803 revision of MELTS for improved calculation of phase relations and major element

- 804 partitioning related to partial melting of the mantle to 3 GPa. *Geochemistry, Geophysics,*
805 *Geosystems*, **3**, Art. No. 1030.
- 806 Goldsmith, J. R., 1980. The melting and breakdown reactions of anorthite at high pressures
807 and temperatures. *American Mineralogist*, **65**, 272–284.
- 808 Goldsmith, J. R. & Jenkins, D. M., 1985. The hydrothermal melting of low and high albite.
809 *American Mineralogist*, **70**, 924–933.
- 810 Goldsmith, J. R. & Peterson, J. W., 1990. Hydrothermal melting behaviour of KAlSi_3O_8 as
811 microcline and sanidine. *American Mineralogist*, **75**, 1362–1369.
- 812 Gottschalk, M., 1996. Internally consistent thermodynamic data for rock-forming minerals
813 in the system $\text{SiO}_2\text{-TiO}_2\text{-Al}_2\text{O}_3\text{-Fe}_2\text{O}_3\text{-CaO-MgO-FeO-K}_2\text{O-Na}_2\text{O-H}_2\text{O-CO}_2$. *European*
814 *Journal of Mineralogy*, **9**, 175–223.
- 815 Grant, J. A., 2009. Thermocalc and experimental modelling of melting of pelite, Morton
816 Pass, Wyoming. *Journal of Metamorphic Geology*, **27**, 571–578.
- 817 Green, E. C. R., Holland, T. J. B. & Powell, R., 2007. An order-disorder model for
818 omphacitic pyroxenes in the system jadeite–diopside–hedenbergite–acmite, with
819 applications to eclogitic rocks. *American Mineralogist*, **92**, 1181–1189.
- 820 Green, E. C. R., Holland, T. J. B. & Powell, R., 2012b. A thermodynamic model for silicate
821 melt in $\text{MgO-Al}_2\text{O}_3\text{-SiO}_2$ and $\text{CaO-MgO-Al}_2\text{O}_3\text{-SiO}_2$ to 50 kbar and 1800 °C. *Journal*
822 *of Metamorphic Geology*, **30**, 579–597.
- 823 Green, E. C. R., Holland, T. J. B., Powell, R. & White, R. W., 2012a. Garnet and spinel
824 lherzolite assemblages in $\text{MgO-Al}_2\text{O}_3\text{-SiO}_2$ and $\text{CaO-MgO-Al}_2\text{O}_3\text{-SiO}_2$: thermodynamic
825 models and an experimental conflict. *Journal of Metamorphic Geology*, **30**, 561–577.
- 826 Gualda, G. A. R., Ghiorso, M. S., Lemons, R. V. & Carley, T. L., 2012. Rhyolite-MELTS:

- 827 A modified calibration of MELTS optimized for silica-rich, fluid-bearing magmatic
828 systems. *Journal of Petrology*, **53**, 875–890.
- 829 Halpin, J. A., Clarke, G. L., White, R. W. & Kelsey, D. E., 2007. Contrasting P–T–t paths
830 for Neoproterozoic metamorphism in MacRobertson and Kemp Lands, east Antarctica.
831 *Journal of Metamorphic Geology*, **25**(6), 683–701.
- 832 Hastie, J. W., 1983. New techniques and opportunities in high-temperature mass
833 spectrometry. *Pure and Applied Chemistry*, **56**, 1583–1600.
- 834 Hastie, J. W. & Bonnell, D. W., 1985. A predictive phase-equilibrium model for
835 multi-component oxide mixtures. 2. Oxides of Na–K–Ca–Mg–Al–Si. *High Temperature*
836 *Science*, **19**, 275–306.
- 837 Holland, T. J. B. & Powell, R., 1996a. Thermodynamics of order-disorder in minerals: I.
838 symmetric formalism applied to minerals of fixed composition. *American*
839 *Mineralogist*, **81**, 1413–1424.
- 840 Holland, T. J. B. & Powell, R., 1996b. Thermodynamics of order-disorder in minerals: II.
841 symmetric formalism applied to solid solutions. *American Mineralogist*, **81**, 1425–1437.
- 842 Holland, T. J. B. & Powell, R., 1998. An internally consistent thermodynamic dataset for
843 phases of petrological interest. *Journal of Metamorphic Geology*, **16**, 309–343.
- 844 Holland, T. J. B. & Powell, R., 2001. Calculation of phase relations involving haplogranitic
845 melts using an internally consistent thermodynamic dataset. *Journal of*
846 *Petrology*, **42**, 673–683.
- 847 Holland, T. J. B. & Powell, R., 2003. Activity–composition relations for phases in
848 petrological calculations: an asymmetric multicomponent formulation. *Contributions to*
849 *Mineralogy and Petrology*, **145**, 492–501.

- 850 Holland, T. J. B. & Powell, R., 2006. Mineral activity–composition relations and
851 petrological calculations involving cation equipartition in multisite minerals: a logical
852 inconsistency. *Journal of Metamorphic Geology*, **24**, 851–861.
- 853 Holland, T. J. B. & Powell, R., 2011. An improved and extended internally consistent
854 thermodynamic dataset for phases of petrological interest, involving a new equation of
855 state for solids. *Journal of Metamorphic Geology*, **29**, 333–383.
- 856 Holland, T. J. B., Hudson, N. F. C., Powell, R. & Harte, B., 2013. New thermodynamic
857 models and calculated phase equilibria in NCFMAS for basic and ultrabasic compositions
858 through the transition zone into the uppermost lower mantle. *Journal of*
859 *Petrology*, **54**, 1901–1920.
- 860 Holtz, F., Behrens, H., Dingwell, D. B. & Johannes, W., 1995. Water solubility in
861 haplogranitic melts. compositional, pressure and temperature dependence. *American*
862 *Mineralogist*, **80**, 94–108.
- 863 Hunt, J. D. & Manning, C. E., 2012. A thermodynamic model for the system $\text{SiO}_2\text{--H}_2\text{O}$
864 near the upper critical end point based on quartz solubility experiments at 500–1100°C
865 and 5–20 kbar. *Geochimica et Cosmochimica Acta*, **86**, 196–213.
- 866 Jackson, I., 1976. Melting of the silica isotypes SiO_2 , BeF_2 and GeO_2 at elevated pressures.
867 *Physics of the Earth and Planetary Interiors*, **13**, 218–231.
- 868 Jakobsson, S., 2012. Oxygen fugacity control in piston-cylinder experiments. *Contributions*
869 *to Mineralogy and Petrology*, **164**, 397–406.
- 870 Jennings, E. S. & Holland, T. J. B., 2015. A simple thermodynamic model for melting of
871 peridotite in the system NCFMASOCr. *Journal of Petrology*, **56**, 1–24.
- 872 Johnson, T. & Brown, M., 2004. Quantitative constraints on metamorphism in the

- 873 Variscides of Southern Brittany—a complementary pseudosection approach. *Journal of*
874 *Petrology*, **45**, 1237–1259.
- 875 Johnson, T. E., White, R. W. & Powell, R., 2008. Partial melting of metagreywacke: a
876 calculated mineral equilibria study. *Journal of Metamorphic Geology*, **26**, 837–853.
- 877 Kelsey, D., White, R., Powell, R., Wilson, C. & Quinn, C., 2003. New constraints on
878 metamorphism in the Rauer Group, Prydz Bay, east Antarctica. *Journal of Metamorphic*
879 *Geology*, **21**(8), 739–759.
- 880 Kennedy, G. C., Wasserburg, G. J., Heard, H. C. & Newton, R. C., 1962. The upper
881 three-phase region in the system $\text{SiO}_2\text{--H}_2\text{O}$. *American Journal of Science*, **260**, 501–521.
- 882 Klemme, S., Ivanic, T. J., Connolly, J. A. D. & Harte, B., 2009. Thermodynamic modelling
883 of Cr-bearing garnets with implications for diamond inclusions and peridotite xenoliths.
884 *Lithos*, **112**, Supplement 2, 986–991.
- 885 Korhonen, F. J., Powell, R. & Stout, J. H., 2012. Stability of sapphirine + quartz in the
886 oxidized rocks of the Wilson Lake terrane, Labrador: calculated equilibria in
887 NCKFMASHTO. *Journal of Metamorphic Geology*, **30**, 21–36.
- 888 Korhonen, F. J., Saito, S., Brown, M. & Siddoway, C. S., 2010. Modeling multiple melt loss
889 events in the evolution of an active continental margin. *Lithos*, **116**, 230–248.
- 890 Kunz, B., Johnson, T., White, R. & Redler, C., 2014. Partial melting of metabasic rocks in
891 Val Strona di Omegna, Ivrea Zone, northern Italy. *Lithos*, **190**, 1–12.
- 892 Lindsley, D., 1966. Melting relations of KAlSi_3O_8 : effect of pressure up to 40 kb. *American*
893 *Mineralogist*, **51**, 1793–1799.
- 894 Lindsley, D., 1981. The formation of pigeonite on the join hedenbergite–ferrosilite at 11.5
895 kbar and 15 kbar: experiments and a solution model. *American*
896 *Mineralogist*, **66**, 1175–1182.

- 897 Lindsley, D., 1983. Pyroxene thermometry. *American Mineralogist*, **68**, 477–493.
- 898 Lindsley, D. & Dixon, S., 1976. Diopside–enstatite equilibria at 850° to 1400°C, 5 to 35 kb.
899 *American Journal of Science*, **276**, 1285–1301.
- 900 London, D., Morgan, G. B. & Acosta-Vigil, A., 2012. Experimental simulations of anatexis
901 and assimilation involving metapelite and granitic melt. *Lithos*, **153**, 292–307.
- 902 López, S. & Castro, A., 2001. Determination of the fluid-absent solidus and supersolidus
903 phase relationships of MORB-derived amphibolites in the range 4–14 kbar. *American*
904 *Mineralogist*, **86**, 1396–1403.
- 905 Manning, C. E., 1994. The solubility of quartz in H₂O in the lower crust and upper mantle.
906 *Geochimica et Cosmochimica Acta*, **58**, 4831–4839.
- 907 Manning, C. E., 2007. Solubility of corundum + kyanite in H₂O at 700° and 10 kbar:
908 evidence for Al–Si complexing at high pressure and temperature. *Geofluids*, **7**, 258–269.
- 909 Matjuschkin, V., Brooker, R. A., Tattitch, B., Blundy, J. D. & Stamper, C. C., 2015.
910 Control and monitoring of oxygen fugacity in piston cylinder experiments. *Contributions*
911 *to Mineralogy and Petrology*, **169**.
- 912 Mori, T. & Green, D. H., 1975. Pyroxenes in the system CaMgSi₂O₆–Mg₂Si₂O₆ at high
913 pressures and temperatures. *American Mineralogist*, **61**, 616–625.
- 914 Newton, R. C. & Haselton, H. T., 1981. Thermodynamics of the
915 garnet–plagioclase–Al₂SiO₅–quartz geobarometer. In: *Thermodynamics of Minerals and*
916 *Melts*, (eds Newton, R. C., Navrotsky, A. & Wood, B. J.), New York, pp. 131–147.
917 Springer Verlag.
- 918 Newton, R. C. & Manning, C. E., 2008. Thermodynamics of SiO₂–H₂O fluid near the upper
919 critical end point from quartz solubility measurements at 10 kbar. *Earth and Planetary*
920 *Science Letters*, **274**, 241–249.

- 921 Nickel, K. G. & Brey, G. P., 1984. Subsolidus orthopyroxene–clinopyroxene systematics in
922 the system CaO–MgO–SiO₂ to 60 kbar: a re-evaluation of the regular solution model.
923 *Contributions to Mineralogy and Petrology*, **87**, 35–42.
- 924 Ostrovsky, I. A., 1966. *PT*-diagram of the system SiO₂–H₂O. *Geological*
925 *Journal*, **5**, 127–134.
- 926 Palin, R. M., Searle, M. P., Waters, D. J., Horstwood, M. S. A. & Parrish, R. R., 2012.
927 Combined thermobarometry and geochronology of peraluminous metapelites from the
928 Karakorum metamorphic complex, North Pakistan; new insight into the tectonothermal
929 evolution of the Baltoro and Hunza regions. *Journal of Metamorphic*
930 *Geology*, **30**, 793–820.
- 931 Palin, R. M., Weller, O. M., Waters, D. J. & Dyck, B., 2016a. Quantifying geological
932 uncertainty in metamorphic phase equilibria modelling: a Monte Carlo assessment and
933 implications for tectonic interpretations. *Geoscience Frontiers*, **7**, 591–607.
- 934 Palin, R. M., White, R. W., Green, E. C. R., Diener, J. F. A., Powell, R. & Holland, T.
935 J. B., 2016b. High-grade metamorphism and partial melting of mafic and intermediate
936 rocks. *Journal of Metamorphic Geology*, **xx**, xxx–xxx.
- 937 Patiño Douce, A. E. & Beard, J. S., 1994. H₂O loss from hydrous melts during fluid-absent
938 piston cylinder experiments. *American Mineralogist*, **79**, 585–588.
- 939 Patiño Douce, A. E. & Beard, J. S., 1995. Dehydration-melting of amphibolite at 10 kbar:
940 the effects of temperature and time. *Journal of Petrology*, **36**, 707–738.
- 941 Perkins, D. & Newton, R. C., 1980. The compositions of coexisting pyroxenes and garnet in
942 the system CaO–MgO–Al₂O₃–SiO₂ at 900°–1,100°C and high pressures. *Contributions to*
943 *Mineralogy and Petrology*, **75**, 291–300.

- 944 Pichavant, M., Mysen, B. O. & MacDonald, R., 2002. Source and H₂O content of high-MgO
945 magmas in island arc settings: an experimental study of a primitive calc-alkaline basalt
946 from St. Vincent, Lesser Antilles arc. *Geochimica et Cosmochimica Acta*, **66**, 2139–2209.
- 947 Powell, R. & Holland, T. J. B., 1988. An internally consistent dataset with uncertainties
948 and correlations: 3. applications to geobarometry, worked examples and a computer
949 program. *Journal of Metamorphic Geology*, **6**, 173–204.
- 950 Powell, R. & Holland, T. J. B., 1993. On the formulation of simple mixing models for
951 complex phases. *American Mineralogist*, **78**, 1174–1180.
- 952 Powell, R. & Holland, T. J. B., 1994. Optimal geothermometry and geobarometry.
953 *American Mineralogist*, **79**, 120–133.
- 954 Powell, R. & Holland, T. J. B., 1999. Relating the formulations of the thermodynamics of
955 mineral solid solutions: activity modeling of pyroxenes, amphiboles, and micas. *American*
956 *Mineralogist*, **84**, 1–14.
- 957 Powell, R. & Holland, T. J. B., 2008. On thermobarometry. *Journal of Metamorphic*
958 *Geology*, **26**, 155–179.
- 959 Powell, R., Holland, T. J. B. & Worley, B., 1998. Calculating phase diagrams involving
960 solid solutions via non-linear equations, with examples using THERMOCALC. *Journal of*
961 *Metamorphic Geology*, **16**, 577–588.
- 962 Qian, Q. & Hermann, J., 2013. Partial melting of lower crust at 10–15 kbar: constraints on
963 adakite and TTG formation. *Contributions to Mineralogy and Petrology*, **165**, 1195–1224.
- 964 Rapp, R. P. & Watson, E. B., 1995. Dehydration melting of metabasalt at 8–32 kbar:
965 implications for continental growth and crust–mantle recycling. *Journal of*
966 *Petrology*, **36**, 891–931.

- 967 Rapp, R. P., Watson, E. B. & Miller, C. F., 1991. Partial melting of amphibolite/eclogite
968 and the origin of Archean trondhjemites and tonalites. *Precambrian Research*, **51**, 1–25.
- 969 Robinson, P., Spear, F. S., Schumacher, J. C., Laird, J., Klein, C., Evans, B. W. & Doolan,
970 B. J., 1982. Phase relations of metamorphic amphiboles: natural occurrence and
971 theory. In: *Reviews in Mineralogy Volume 9B: Amphiboles: Petrology and Experimental*
972 *Phase Relations*, (eds Veblen, D. R. & Ribbe, P. H.), pp. 1–288. Mineralogical Society of
973 America.
- 974 Rushmer, T., 1991. Partial melting of two amphibolites: contrasting experimental results
975 under fluid-absent conditions. *Contributions to Mineralogy and Petrology*, **107**, 41–59.
- 976 Schumacher, J. C., 2007. Metamorphic amphiboles: composition and coexistence. In:
977 *Reviews in Mineralogy Volume 67: Amphiboles: Crystal Chemistry, Occurrence, and*
978 *Health issues*, (eds Hawthorne, F. C., Oberti, R., Della Ventura, G. & Mottana, A.),
979 pp. 359–416. Mineralogical Society of America.
- 980 Schweitzer, E., 1982. The reaction pigeonite = diopside_{ss} + enstatite_{ss} at 15 kbar. *American*
981 *Mineralogist*, **67**, 54–58.
- 982 Sen, C. & Dunn, T., 1994. Dehydration melting of a basaltic composition amphibolite at
983 1.5 and 2.0 GPa: implications for the origin of adakites. *Contributions to Mineralogy and*
984 *Petrology*, **117**, 394–409.
- 985 Skjerlie, K. P. & Patiño Douce, A. E., 1995. Anatexis of interlayered amphibolite and pelite
986 and 10 kbar: effect of diffusion of major components on phase relations and melt fraction.
987 *Contributions to Mineralogy and Petrology*, **122**, 62–78.
- 988 Skjerlie, K. P. & Patiño Douce, A. E., 2002. The fluid-absent partial melting of a
989 zoisite-bearing quartz eclogite from 1.0 to 3.2 GPa; implications for melting in thickened
990 continental crust and for subduction-zone processes. *Journal of Petrology*, **43**, 291–314.

- 991 Smith, P. M. & Asimow, P. D., 2005. Adibat-1ph: A new public front-end to the MELTS,
992 pMELTS and pHMELTS. *Geochemistry, Geophysics, Geosystems*, **6**, Q02004.
- 993 Springer, W. & Seck, H. A., 1997. Partial fusion of basic granulites at 5 to 15 kbar:
994 implications for the origin of TTG magmas. *Contributions to Mineralogy and*
995 *Petrology*, **127**, 30–45.
- 996 Stewart, D. B., 1967. Four phase curve in the system $\text{CaAl}_2\text{Si}_2\text{O}_8\text{--SiO}_2\text{--H}_2\text{O}$.
997 *Schweizerische Mineralogische und Petrologische Mitteilungen*, **47**, 35–39.
- 998 Stormer, J. C., 1975. A practical two-feldspar geothermometer. *American*
999 *Mineralogist*, **60**, 667–674.
- 1000 Streule, M. J., Searle, M. P., Waters, D. J. & Horstwood, M. S. A., 2010. Metamorphism,
1001 melting, and channel flow in the Greater Himalayan Sequence and Makalu leucogranite:
1002 constraints from thermobarometry, metamorphic modeling, and U–Pb geochronology.
1003 *Tectonics*, **29**, TC5011.
- 1004 Sun, S. S. & McDonough, W. F., 1989. Chemical and isotopic systematics of oceanic basalts:
1005 implications for mantle compositions and processes. In: *Magmatism in the Ocean Basins*,
1006 (eds Saunders, A. D. & Norry, M. J.), Vol. 42, pp. 313–345. Geological Society of London.
- 1007 Thompson, A. B., 1976. Mineral reactions in pelitic rocks: II. Calculation of some
1008 P–T–X(Fe–Mg) phase relations. *American Journal of Science*, **276**, 425–454.
- 1009 Truckenbrodt, J. & Johannes, W., 1999. H_2O loss during piston-cylinder experiments.
1010 *American Mineralogist*, **84**, 1333–1335.
- 1011 Turnock, A. C. & Lindsley, D. H., 1981. Experimental determination of pyroxene solvi for
1012 ≤ 1 kbar at 900 and 1000°C. *Canadian Mineralogist*, **19**, 255–267.
- 1013 van Laar, J. J., 1906. *Sechs Vorträge über das thermodynamischer Potential*, Vieweg,
1014 Brunswick.

- 1015 White, R. W., Powell, R. & Clarke, G. L., 2002. The interpretation of reaction textures in
1016 Fe-rich metapelitic granulites of the Musgrave Block, central Australia: constraints from
1017 mineral equilibria calculations in the system
1018 $K_2O-FeO-MgO-Al_2O_3-SiO_2-H_2O-TiO_2-Fe_2O_3$. *Journal of Metamorphic*
1019 *Geology*, **20**, 41–55.
- 1020 White, R. W., Powell, R. & Clarke, G. L., 2003. Prograde metamorphic assemblage
1021 evolution during partial melting of metasedimentary rocks at low pressures: Migmatites
1022 from Mt Stafford, central Australia. *Journal of Petrology*, **44**, 1937–1960.
- 1023 White, R. W., Powell, R. & Holland, T. J. B., 2001. Calculation of partial melting
1024 equilibria in the system $Na_2O-CaO-K_2O-FeO-MgO-Al_2O_3-SiO_2-H_2O$ (NCKFMASH).
1025 *Journal of Metamorphic Geology*, **19**, 139–153.
- 1026 White, R. W., Powell, R. & Holland, T. J. B., 2007. Progress relating to calculation of
1027 partial melting equilibria for metapelites. *Journal of Metamorphic Geology*, **25**, 511–527.
- 1028 White, R. W., Powell, R., Holland, T. J. B. & Worley, B. A., 2000. The effect of TiO_2 and
1029 Fe_2O_3 on metapelitic assemblages at greenschist and amphibolite facies conditions:
1030 mineral equilibria calculations in the system
1031 $K_2O-FeO-MgO-Al_2O_3-SiO_2-H_2O-TiO_2-Fe_2O_3$. *Journal of Metamorphic*
1032 *Geology*, **18**, 497–511.
- 1033 White, R. W., Powell, R., Holland, T. J. B., Johnson, T. E. & Green, E. C. R., 2014.
1034 Progress relating to calculation of partial melting equilibria for metapelites. *Journal of*
1035 *Metamorphic Geology*, **25**, 511–527.
- 1036 White, R. W., Stevens, G. & Johnson, T. E., 2011. Is the crucible reproducible?
1037 Reconciling melting experiments with thermodynamic calculations. *Elements*, **7**, 241–246.
- 1038 Wolf, M. B. & Wyllie, P. J., 1994. Dehydration-melting of amphibolite at 10 kbar: the

- 1039 effects of temperature and time. *Contributions to Mineralogy and*
1040 *Petrology*, **115**, 369–383.
- 1041 Wood, B. J. & Banno, S., 1973. Garnet–orthopyroxene and orthopyroxene–clinopyroxene
1042 relationships in simple and complex systems. *Contributions to Mineralogy and*
1043 *Petrology*, **42**, 109–124.
- 1044 Yoder, H. S., 1976. Melting of the silica isotypes SiO₂, BeF₂ and GeO₂ at elevated
1045 pressures. *Carnegie Institution of Washington Yearbook*, **64**, 82–89.
- 1046 Zhang, C., Holtz, F., Koepke, J., Wolff, P. E., Ma, C. & Bédard, J. H., 2013. Constraints
1047 from experimental melting of amphibolite on the depth of formation of garnet-rich
1048 restites, and implications for models of Early Archean crustal growth. *Precambrian*
1049 *Research*, **231**, 206–217.
- 1050 Ziaja, K., Foley, S. F., White, R. W. & Buhre, S., 2014. Metamorphism and melting of
1051 picritic crust in the early Earth. *Lithos*, **189**, 173–184.

1052 APPENDIX

1053 The thermodynamic models discussed in this paper may be conveniently used with the
1054 software THERMOCALC (Powell & Holland, 1988). The THERMOCALC software may be
1055 downloaded from the University of Mainz THERMOCALC website at
1056 <http://www.metamorph.geo.uni-mainz.de/thermocalc/>, along with input files containing
1057 the $a-x$ relations, versions of the Holland & Powell (2011) dataset, and explanatory notes.
1058 THERMOCALC versions tc340 and above should be used. Versions ds62 and ds63 of the
1059 Holland & Powell (2011) dataset have not been formally published, so anyone wishing to
1060 use them independently of THERMOCALC must extract parameters from the THERMOCALC
1061 input files. To assist in doing so, THERMOCALC may be run in mode 0 with the appropriate
1062 dataset and $a-x$ relations, generating tables of G values as functions of P and T for each
1063 end-member, including those that do not appear explicitly in the dataset. The G values
1064 include any ΔG_i expressions applied to the end-members (identified in $a-x$ input files by
1065 the script 'DQF').

1066 Full thermodynamic descriptions of the new $a-x$ relations for clinopyroxene (augite
1067 model), clinoamphibole and metabasite melt are given below. ΔG_i terms are specified
1068 relative to end-members that appear in the Holland & Powell (2011) dataset. Interaction
1069 energies $W_{i,j}$ and ΔG_i parameters are specified as functions of pressure P in kilobar and T
1070 in kelvin: $W_{i,j} = W_{i,j}^a + W_{i,j}^b T + W_{i,j}^c P$ and $\Delta G_i = \Delta G_i^a + \Delta G_i^b T + \Delta G_i^c P$.

1071 Clinopyroxene models

1072 In the augite model, the following independent set of end-members is used, with the cations
1073 shown on their mixing sites, and the tetrahedral site split into T1 and T2 in order to
1074 describe Si–Al ordering in the cats end-member (the latter is an intrinsic property of the
1075 cats end-member of the Holland & Powell (2011) dataset, written out explicitly in the $a-x$
1076 model):

	M1				M2				T1		T2	
	Mg	Fe	Al	Fe3	Mg	Fe	Ca	Na	Si	Al	Si	Al
di	1	0	0	0	0	0	1	0	1	0	1	0
cenh	1	0	0	0	1	0	0	0	1	0	1	0
cfs	0	1	0	0	0	1	0	0	1	0	1	0
jd	0	0	1	0	0	0	0	1	1	0	1	0
acm	0	0	0	1	0	0	0	1	1	0	1	0
ocats	0	0	1	0	0	0	1	0	1	0	0	1
dcats	0	0	1	0	0	0	1	0	$\frac{1}{2}$	$\frac{1}{2}$	$\frac{1}{2}$	$\frac{1}{2}$
fmc	1	0	0	0	0	1	0	0	1	0	1	0

1078 Cen_h and cfs are the *C2/c* polymorphs of the dataset *Pbca* end-members en and fs, and are
1079 derived from them via $\Delta G_{\text{cenh}}^{\text{tran}} = G_{\text{cenh}} - G_{\text{en}} = 3.5 - 0.002T + 0.048P$ kJ and $\Delta G_{\text{cfs}}^{\text{tran}} =$
1080 $G_{\text{cfs}} - G_{\text{fs}} = 2.1 - 0.002T + 0.045P$ kJ. Fmc is the ordered end-member for which $G_{\text{fmc}} =$
1081 $\frac{1}{2}(G_{\text{cenh}} + G_{\text{cfs}}) + \Delta G_{\text{ordering}}$. Because ΔG_i terms are described relative to dataset
1082 end-members, $\Delta G_{\text{fmc}}^{\text{od}}$ incorporates $\Delta G_{\text{ordering}}$, $\Delta G_{\text{cenh}}^{\text{tran}}$ and $\Delta G_{\text{cfs}}^{\text{tran}}$: $\Delta G_{\text{fmc}}^{\text{od}} = \frac{1}{2}(\Delta G_{\text{cenh}}^{\text{tran}} +$
1083 $\Delta G_{\text{cfs}}^{\text{tran}}) + \Delta G_{\text{ordering}} = -1.6 - 0.002T + 0.0465P$ kJ. Ocats and dcats are the fully ordered
1084 and fully disordered forms respectively of the dataset cats end-member. Together they
1085 reproduce the thermodynamics of the cats end-member via prescribed values for $W_{\text{ocats,dcats}}$
1086 and the term $\Delta G_{\text{dcats}} = 3.8 - 0.0028816T + 0.01P$ kJ. $W_{\text{ocats,dcats}}$, $\Delta G_{\text{dcats}}^a$ and $\Delta G_{\text{dcats}}^c$ can
1087 be found in Holland & Powell (2011), table 2c, while $\Delta G_{\text{dcats}}^b$ represents the configurational
1088 entropy involved in disordering. Jd and acm are subject to ΔG_i^{mod} terms of 2 kJ and -5 kJ
1089 respectively.

1090 Composition is described by the variables

$$\begin{aligned}
 x &= \frac{\text{Fe}}{\text{Fe} + \text{Mg}} \\
 &= \frac{x_{\text{Fe}}^{\text{M1}} + x_{\text{Fe}}^{\text{M2}}}{x_{\text{Fe}}^{\text{M1}} + x_{\text{Fe}}^{\text{M2}} + x_{\text{Mg}}^{\text{M1}} + x_{\text{Mg}}^{\text{M2}}} \\
 y &= \frac{x_{\text{Al}}^{\text{T1}} + x_{\text{Al}}^{\text{T2}}}{x_{\text{Al}}^{\text{T1}} + x_{\text{Al}}^{\text{T2}}} \\
 f &= \frac{x_{\text{Fe3}}^{\text{M1}}}{x_{\text{Fe3}}^{\text{M1}}} \\
 z &= \frac{x_{\text{Ca}}^{\text{M2}}}{x_{\text{Ca}}^{\text{M2}}} \\
 j &= \frac{x_{\text{Na}}^{\text{M2}}}{x_{\text{Na}}^{\text{M2}}},
 \end{aligned}$$

1091 and order-disorder by the parameters

$$Q_{fm} = 2 \left(\frac{x_{\text{Fe}}^{\text{M2}}}{x_{\text{Fe}}^{\text{M2}} + x_{\text{Mg}}^{\text{M2}}} - x \right)$$

$$Q_{al} = x_{\text{Al}}^{\text{T2}} - x_{\text{Al}}^{\text{T1}},$$

1092 which are found by solving the internal equilibria via which the corresponding order-disorder
1093 end-members are formed, i.e. $\text{fmc} = \frac{1}{2} (\text{cenh} + \text{cfs})$ and $\text{dcats} = \text{ocats}$. The site fractions are

$$x_{\text{Mg}}^{\text{M1}} = 1 - j - x - y + jx + xy + \frac{Q_{fm}}{2} (1 - j - z)$$

$$x_{\text{Fe}}^{\text{M1}} = x - jx - xy - \frac{Q_{fm}}{2} (1 - j - z)$$

$$x_{\text{Al}}^{\text{M1}} = j + y - f$$

$$x_{\text{Fe3}}^{\text{M1}} = f$$

$$x_{\text{Mg}}^{\text{M2}} = 1 - j - x - z - \frac{Q_{fm}}{2} (1 - j - z) + jx + xz$$

$$x_{\text{Fe}}^{\text{M2}} = x + \frac{Q_{fm}}{2} (1 - j - z) - jx - xz$$

$$x_{\text{Ca}}^{\text{M2}} = z$$

$$x_{\text{Na}}^{\text{M2}} = j$$

$$x_{\text{Si}}^{\text{T1}} = 1 - \frac{1}{2} (y - Q_{al})$$

$$x_{\text{Al}}^{\text{T1}} = \frac{1}{2} (y - Q_{al})$$

$$x_{\text{Si}}^{\text{T2}} = 1 - \frac{1}{2} (y + Q_{al})$$

$$x_{\text{Al}}^{\text{T2}} = \frac{1}{2} (y + Q_{al}),$$

1094 and the ideal activities are

$$a_{\text{di}}^{\text{ideal}} = x_{\text{Mg}}^{\text{M1}} x_{\text{Ca}}^{\text{M2}} (x_{\text{Si}}^{\text{T1}} x_{\text{Si}}^{\text{T2}})^{\frac{1}{4}}$$

$$a_{\text{cenh}}^{\text{ideal}} = x_{\text{Mg}}^{\text{M1}} x_{\text{Mg}}^{\text{M2}} (x_{\text{Si}}^{\text{T1}} x_{\text{Si}}^{\text{T2}})^{\frac{1}{4}}$$

$$a_{\text{cfs}}^{\text{ideal}} = x_{\text{Fe}}^{\text{M1}} x_{\text{Fe}}^{\text{M2}} (x_{\text{Si}}^{\text{T1}} x_{\text{Si}}^{\text{T2}})^{\frac{1}{4}}$$

$$\begin{aligned}
a_{jd}^{\text{ideal}} &= x_{\text{Al}}^{\text{M1}} x_{\text{Na}}^{\text{M2}} \left(x_{\text{Si}}^{\text{T1}} x_{\text{Si}}^{\text{T2}} \right)^{\frac{1}{4}} \\
a_{\text{acm}}^{\text{ideal}} &= x_{\text{Fe3}}^{\text{M1}} x_{\text{Na}}^{\text{M2}} \left(x_{\text{Si}}^{\text{T1}} x_{\text{Si}}^{\text{T2}} \right)^{\frac{1}{4}} \\
a_{\text{ocats}}^{\text{ideal}} &= x_{\text{Al}}^{\text{M1}} x_{\text{Ca}}^{\text{M2}} \left(x_{\text{Si}}^{\text{T1}} x_{\text{Al}}^{\text{T2}} \right)^{\frac{1}{4}} \\
a_{\text{dcats}}^{\text{ideal}} &= \sqrt{2} x_{\text{Al}}^{\text{M1}} x_{\text{Ca}}^{\text{M2}} \left(x_{\text{Si}}^{\text{T1}} x_{\text{Al}}^{\text{T1}} x_{\text{Si}}^{\text{T2}} x_{\text{Al}}^{\text{T2}} \right)^{\frac{1}{8}} \\
a_{\text{fmc}}^{\text{ideal}} &= x_{\text{Mg}}^{\text{M1}} x_{\text{Fe}}^{\text{M2}} \left(x_{\text{Si}}^{\text{T1}} x_{\text{Si}}^{\text{T2}} \right)^{\frac{1}{4}},
\end{aligned}$$

1095 including the entropy reduction factor. Non-ideal activities are given by equation 2. The
1096 end-member proportions for use in equation 2 are

$$\begin{aligned}
p_{\text{di}} &= z - y \\
p_{\text{cenh}} &= 1 - j - x - z - \frac{Q_{\text{fm}}}{2} (1 - j - z) + jx + xz \\
p_{\text{cfs}} &= x - \frac{Q_{\text{fm}}}{2} (1 - j - z) - jx - xy \\
p_{\text{jd}} &= j - f \\
p_{\text{acm}} &= f \\
p_{\text{ocats}} &= Q_{\text{al}} \\
p_{\text{dcats}} &= y - Q_{\text{al}} \\
p_{\text{fmc}} &= Q_{\text{fm}} (1 - j - z) + xy - xz.
\end{aligned}$$

1097 The interaction energies are:

1098

$W_{i,j}$ (kJ)	cenh	cfs	jd	acm	ocats	dcats	fmc
di	29.8 - 0.03P	25.8 - 0.03P	26	21	12.3 - 0.01P	12.3 - 0.01P	20.6 - 0.03P
cenh		2.3	50	62	45.7 - 0.29P	45.7 - 0.29P	4
cfs			60	58	48	48	3.5
1099 jd				5	40	40	40
acm					35	35	60
ocats						3.8 + 0.01P	50
dcats							50

1100 with asymmetry introduced by the van Laar parameters $\alpha_{\text{cenh}} = \alpha_{\text{cfs}} = \alpha_{\text{fmc}} = 1$, $\alpha_{\text{di}} = \alpha_{\text{jd}}$
 1101 $= \alpha_{\text{acm}} = 1.2$, and $\alpha_{\text{ocats}} = \alpha_{\text{dcats}} = 1.9$.

1102 We reiterate that the augite model does not have a structure suitable for calculations
 1103 where coexisting clinopyroxenes may be expected. To calculate two-clinopyroxene
 1104 equilibria, the ‘omphacite’ model should be used for both phases, using appropriate starting
 1105 guesses for the compositional parameters in each. The omphacite model is described in
 1106 Green *et al.* (2007), with new $W_{\text{acm},n}$ values given in Diener & Powell (2012) and a new
 1107 value for $\Delta G_{\text{acm}}^{\text{mod}}$, of -7 kJ, given in this paper. The change to $\Delta G_{\text{acm}}^{\text{mod}}$ entails a
 1108 corresponding change to the parameter $\Delta G_{\text{jac}}^{\text{od}}$. The jac end-member is the ordered
 1109 intermediate $\text{Na}_{\frac{1}{2}}^{\text{M2}}\text{Na}_{\frac{1}{2}}^{\text{M1}}\text{Fe}_{\frac{1}{2}}^{3+\text{M1}}\text{Al}_{\frac{1}{2}}^{\text{M1}}\text{Si}_2^{\text{tet}}\text{O}_6$, and is formed through the reaction $\text{jac} = \frac{1}{2}(\text{jd}$
 1110 $+ \text{acm}) + \Delta G_{\text{jac}}^{\text{od}}$, such that $\Delta G_{\text{jac}}^{\text{od}} = \frac{1}{2}(\Delta G_{\text{jd}}^{\text{mod}} + \Delta G_{\text{acm}}^{\text{mod}}) - 1$ kJ. With $\Delta G_{\text{jd}}^{\text{mod}} = 0$, the
 1111 change to $\Delta G_{\text{acm}}^{\text{mod}}$ leads to $\Delta G_{\text{jac}}^{\text{od}} = -4.5$ kJ, rather than the previous value of -5 kJ.

1112 For comparison between the omphacite and augite models, the dependent parameters
 1113 associated with the hed end-member, $\text{CaFeSi}_2\text{O}_6$, in the augite model are compared here
 1114 with their equivalents in the omphacite model.

parameter (kJ)	augite model	omphacite model
$W_{\text{di,hed}}$	2.9	4
$W_{\text{cenh,hed}}$	$26.6 - 0.03P$	-
$W_{\text{cfs,hed}}$	$20.9 - 0.03P$	-
$W_{\text{jd,hed}}$	42.4	24
$W_{\text{acm,hed}}$	17.4	20.8
$W_{\text{ocats,hed}}, W_{\text{dcats,hed}}$	$8.7 - 0.01P$	-
ΔG_{hed} at 8 kbar, 900°C	1.5	0

1116 There is however no discordance of symmetry between the two models, as they both feature
 1117 $\alpha_{\text{di}} = \alpha_{\text{jd}} = \alpha_{\text{acm}} = \alpha_{\text{hed}}$. For the method of determining the dependency relationships, see
 1118 Powell & Holland (1999).

1119 Clinoamphibole model

1120 The following independent set of end-members is used, based on an amphibole formula

1121 calculated for 23 oxygen atoms, with the mixing sites only shown (v=vacancy):

1122

	A		M13			M2			M4				T1		V			
	v	Na	K	Mg	Fe	Mg	Fe	Al	Fe3	Ti	Ca	Mg	Fe	Na	Si	Al	OH	O
tr	1	0	0	3	0	2	0	0	0	0	2	0	0	0	4	0	2	0
ts	1	0	0	3	0	0	0	2	0	0	2	0	0	0	2	2	2	0
parg	0	1	0	3	0	1	0	1	0	0	2	0	0	0	2	2	2	0
gl	1	0	0	3	0	0	0	2	0	0	0	0	0	2	4	0	2	0
1123 cumm	1	0	0	3	0	2	0	0	0	0	0	2	0	0	4	0	2	0
grun	1	0	0	0	3	0	2	0	0	0	0	0	2	0	4	0	2	0
a	1	0	0	3	0	0	2	0	0	0	0	0	2	0	4	0	2	0
b	1	0	0	0	3	2	0	0	0	0	0	0	2	0	4	0	2	0
mrbs	1	0	0	3	0	0	0	0	2	0	0	0	0	2	4	0	2	0
kprg	0	0	1	3	0	1	0	1	0	0	2	0	0	0	2	2	2	0
tts	1	0	0	3	0	0	0	0	0	2	2	0	0	0	2	2	0	2

1124 As the end-member thermodynamics are in general not well known, it is assumed that that
1125 dataset end-member tr is correct, while the other compositional end-members ts, parg, gl,
1126 cumm and grun are modified relative to this via terms $\Delta G_{ts}^{\text{mod}} = 10$ kJ, $\Delta G_{\text{parg}}^{\text{mod}} = -10$ kJ,
1127 $\Delta G_{\text{gl}}^{\text{mod}} = -3$ kJ, $\Delta G_{\text{cumm}}^{\text{mod}} = 0$ kJ, $\Delta G_{\text{grun}}^{\text{mod}} = -3$ kJ. Order-disorder of Fe-Mg on the M13,
1128 M2 and M4 sites is governed by end-members $a = \frac{3}{7}$ cumm + $\frac{4}{7}$ grun + ΔG_a^{od} and $b = \frac{2}{7}$
1129 cumm + $\frac{5}{7}$ grun + ΔG_b^{od} , where the ΔG relative to the dataset values of the end-members
1130 are given by $\Delta G_a^{\text{od}} = \frac{3}{7} \Delta G_{\text{cumm}}^{\text{mod}} + \frac{4}{7} \Delta G_{\text{grun}}^{\text{mod}} - 9.5 = -11.2$ kJ and $\Delta G_b^{\text{od}} = \frac{2}{7} \Delta G_{\text{cumm}}^{\text{mod}} + \frac{5}{7}$
1131 $\Delta G_{\text{grun}}^{\text{mod}} - 11.7 = -13.8$ kJ. The ferric end-member mrbs, and the new end-members kprg and
1132 tts, have to be 'made' from dataset end-members via the reactions $\text{mrbs} = \text{gl} - \text{gr} + \text{andr} +$
1133 $\Delta G_{\text{mrbs}}^{\text{make}}$, $\text{kprg} = \text{mu} - \text{pa} + \text{parg} + \Delta G_{\text{kprg}}^{\text{make}}$, and $\text{tts} = \text{ts} + 2 \text{ru} - 2 \text{dsp} + \Delta G_{\text{tts}}^{\text{make}}$
1134 respectively, where the dG terms are $\Delta G_{\text{mrbs}}^{\text{make}} = 0$ kJ, $\Delta G_{\text{kprg}}^{\text{make}} = -7.06 + 0.02 T$ kJ and
1135 $\Delta G_{\text{tts}}^{\text{make}} = 95$ kJ (gr: grossular; andr: andradite; mu: muscovite; pa: paragonite; ru: rutile;
1136 dsp: diaspore). Diener *et al.* (2007) describe the structure and calibration of the core
1137 NCFMASHO model more fully.

1138 Composition and order are described by the variables

$$x = \frac{\text{Fe}}{\text{Fe} + \text{Mg}}$$

$$\begin{aligned}
&= \frac{3x_{\text{Fe}}^{\text{M13}} + 2x_{\text{Fe}}^{\text{M2}} + 2x_{\text{Fe}}^{\text{M4}}}{3x_{\text{Fe}}^{\text{M13}} + 2x_{\text{Fe}}^{\text{M2}} + 2x_{\text{Fe}}^{\text{M4}} + 3x_{\text{Mg}}^{\text{M13}} + 2x_{\text{Mg}}^{\text{M2}} + 2x_{\text{Mg}}^{\text{M4}}} \\
y &= x_{\text{Al}}^{\text{M2}} \\
z &= x_{\text{Na}}^{\text{M4}} \\
a &= x_{\text{K}}^{\text{A}} + x_{\text{Na}}^{\text{A}} \\
k &= \frac{x_{\text{K}}^{\text{A}}}{x_{\text{K}}^{\text{A}} + x_{\text{Na}}^{\text{K}}} \\
c &= x_{\text{Ca}}^{\text{M4}} \\
f &= x_{\text{Fe3}}^{\text{M2}} \\
t &= x_{\text{Ti}}^{\text{M2}} \\
Q_1 &= x - \frac{x_{\text{Fe}}^{\text{M13}}}{x_{\text{Fe}}^{\text{M13}} + x_{\text{Mg}}^{\text{M13}}} \\
Q_2 &= x - \frac{x_{\text{Fe}}^{\text{M2}}}{x_{\text{Fe}}^{\text{M2}} + x_{\text{Mg}}^{\text{M2}}}.
\end{aligned}$$

1139 The site fractions are

$$\begin{aligned}
x_{\text{v}}^{\text{A}} &= 1 - a \\
x_{\text{Na}}^{\text{A}} &= a(1 - k) \\
x_{\text{K}}^{\text{A}} &= ak \\
x_{\text{Mg}}^{\text{M13}} &= 1 - x + Q_1 \\
x_{\text{Fe}}^{\text{M13}} &= x - Q_1 \\
x_{\text{Mg}}^{\text{M2}} &= 1 - x - y - f - t + Q_2(1 - f - t - y) + fx + tx + xy \\
x_{\text{Fe}}^{\text{M2}} &= x - Q_2(1 - f - t - y) - fx - tx - xy \\
x_{\text{Al}}^{\text{M2}} &= y \\
x_{\text{Fe3}}^{\text{M2}} &= f \\
x_{\text{Ti}}^{\text{M2}} &= t \\
x_{\text{Ca}}^{\text{M4}} &= c \\
x_{\text{Mg}}^{\text{M4}} &= 1 - c - x - z - \frac{3Q_1}{2} - Q_2(1 - f - t - y) + xc + xz
\end{aligned}$$

$$x_{\text{Fe}}^{\text{M4}} = x + \frac{3Q_1}{2} + Q_2(1 - f - t - y) - xc - xz$$

$$x_{\text{Na}}^{\text{M4}} = z$$

$$x_{\text{Si}}^{\text{T1}} = 1 - \frac{1}{2} \left(f + t + y - z + \frac{1}{2}a \right)$$

$$x_{\text{Al}}^{\text{T1}} = \frac{1}{2} \left(f + t + y - z + \frac{1}{2}a \right)$$

$$x_{\text{OH}}^{\text{V}} = 1 - t$$

$$x_{\text{O}}^{\text{V}} = t$$

1140 and ideal activities

$$a_{\text{tr}}^{\text{ideal}} = x_{\text{v}}^{\text{A}} (x_{\text{Mg}}^{\text{M13}})^3 (x_{\text{Mg}}^{\text{M2}})^2 (x_{\text{Ca}}^{\text{M4}})^2 x_{\text{Si}}^{\text{T1}} (x_{\text{OH}}^{\text{V}})^2$$

$$a_{\text{ts}}^{\text{ideal}} = 2 x_{\text{v}}^{\text{A}} (x_{\text{Mg}}^{\text{M13}})^3 (x_{\text{Mg}}^{\text{M2}})^2 (x_{\text{Ca}}^{\text{M4}})^2 (x_{\text{Si}}^{\text{T1}})^{\frac{1}{2}} (x_{\text{Al}}^{\text{T1}})^{\frac{1}{2}} (x_{\text{OH}}^{\text{V}})^2$$

$$a_{\text{parg}}^{\text{ideal}} = 8 x_{\text{Na}}^{\text{A}} (x_{\text{Mg}}^{\text{M13}})^3 x_{\text{Mg}}^{\text{M2}} x_{\text{Al}}^{\text{M2}} (x_{\text{Ca}}^{\text{M4}})^2 (x_{\text{Si}}^{\text{T1}})^{\frac{1}{2}} (x_{\text{Al}}^{\text{T1}})^{\frac{1}{2}} (x_{\text{OH}}^{\text{V}})^2$$

$$a_{\text{gl}}^{\text{ideal}} = x_{\text{v}}^{\text{A}} (x_{\text{Mg}}^{\text{M13}})^3 (x_{\text{Al}}^{\text{M2}})^2 (x_{\text{Na}}^{\text{M4}})^2 x_{\text{Si}}^{\text{T1}} (x_{\text{OH}}^{\text{V}})^2$$

$$a_{\text{cumm}}^{\text{ideal}} = x_{\text{v}}^{\text{A}} (x_{\text{Mg}}^{\text{M13}})^3 (x_{\text{Mg}}^{\text{M2}})^2 (x_{\text{Mg}}^{\text{M4}})^2 x_{\text{Si}}^{\text{T1}} (x_{\text{OH}}^{\text{V}})^2$$

$$a_{\text{grun}}^{\text{ideal}} = x_{\text{v}}^{\text{A}} (x_{\text{Fe}}^{\text{M13}})^3 (x_{\text{Fe}}^{\text{M2}})^2 (x_{\text{Fe}}^{\text{M4}})^2 x_{\text{Si}}^{\text{T1}} (x_{\text{OH}}^{\text{V}})^2$$

$$a_{\text{a}}^{\text{ideal}} = x_{\text{v}}^{\text{A}} (x_{\text{Mg}}^{\text{M13}})^3 (x_{\text{Fe}}^{\text{M2}})^2 (x_{\text{Fe}}^{\text{M4}})^2 x_{\text{Si}}^{\text{T1}} (x_{\text{OH}}^{\text{V}})^2$$

$$a_{\text{b}}^{\text{ideal}} = x_{\text{v}}^{\text{A}} (x_{\text{Fe}}^{\text{M13}})^3 (x_{\text{Mg}}^{\text{M2}})^2 (x_{\text{Fe}}^{\text{M4}})^2 x_{\text{Si}}^{\text{T1}} (x_{\text{OH}}^{\text{V}})^2$$

$$a_{\text{mrb}}^{\text{ideal}} = x_{\text{v}}^{\text{A}} (x_{\text{Mg}}^{\text{M13}})^3 (x_{\text{Fe3}}^{\text{M2}})^2 (x_{\text{Na}}^{\text{M4}})^2 x_{\text{Si}}^{\text{T1}} (x_{\text{OH}}^{\text{V}})^2$$

$$a_{\text{kprg}}^{\text{ideal}} = 8 x_{\text{K}}^{\text{A}} (x_{\text{Mg}}^{\text{M13}})^3 x_{\text{Mg}}^{\text{M2}} x_{\text{Al}}^{\text{M2}} (x_{\text{Ca}}^{\text{M4}})^2 (x_{\text{Si}}^{\text{T1}})^{\frac{1}{2}} (x_{\text{Al}}^{\text{T1}})^{\frac{1}{2}} (x_{\text{OH}}^{\text{V}})^2$$

$$a_{\text{tts}}^{\text{ideal}} = 2 x_{\text{v}}^{\text{A}} (x_{\text{Mg}}^{\text{M13}})^3 (x_{\text{Ti}}^{\text{M2}})^2 (x_{\text{Ca}}^{\text{M4}})^2 (x_{\text{Si}}^{\text{T1}})^{\frac{1}{2}} (x_{\text{Al}}^{\text{T1}})^{\frac{1}{2}} (x_{\text{O}}^{\text{V}})^2,$$

1141 with non-ideal activities given by equation (2). The end-member proportions are

$$p_{\text{tr}} = c + z - \frac{a}{2} - f - t - y$$

$$p_{\text{ts}} = y + f - z - \frac{a}{2}$$

$$p_{\text{parg}} = a(1 - k)$$

$$\begin{aligned}
p_{gl} &= z - f \\
p_{cumm} &= 1 - c - x - z - \frac{3Q_1}{2} - Q_2(1 - f - t - y) + cx + xz \\
p_{grun} &= x - \frac{5Q_1}{2} - 2Q_2(1 - f - t - y) + cx - fx - tx - xy + xz \\
p_a &= \frac{5Q_2}{2} + Q_2(1 - f - t - y) - xc - xz \\
p_b &= \frac{3Q_1}{2} + 2Q_2(1 - f - t - y) - xc + fx + tx + xy - xz \\
p_{mrb} &= f \\
p_{kprg} &= ak \\
p_{tts} &= t.
\end{aligned}$$

1142 The interaction energies are:

W_{ij} (kJ)	ts	parg	gl	cumm	grun	a	b	mrb	kprg	tts
tr	20	25	65	45	75	57	63	52	30	85
ts		-40	25	70	80	70	72.5	20	-40	35
parg			50	90	106.7	94.8	94.8	40	8	15
gl				100	113.5	100	111.2	0	54	75
1143 cumm					33	18	23	80	87	100
grun						12	8	91	96	65
a							20	80	94	95
b								90	94	95
mrb									50	50
kprg										35

1144 with asymmetry introduced by the van Laar parameters $\alpha_{tr} = \alpha_{cumm} = \alpha_{grun} = \alpha_a = \alpha_b =$

1145 1 , $\alpha_{ts} = \alpha_{tts} = 1.5$, $\alpha_{gl} = \alpha_{mrb} = 0.8$, and $\alpha_{parg} = \alpha_{kprg} = 1.7$.

1146 These $a-x$ relations are suitable for all of the clin amphibole solid solutions hornblende,
1147 glaucophane, actinolite and cummingtonite, when appropriate starting guesses are given for
1148 the compositional variables.

1149 Melt model

1150 The end-members are mixing units with mineral-like formulae:

end-member	formula
qL	Si ₄ O ₈
abL	NaAlSi ₃ O ₈
kspL	KAlSi ₃ O ₈
woL	CaSiO ₃
1151 silL	Al ₂ SiO ₅
faL	Fe ₄ Si ₂ O ₈
foL	Mg ₄ Si ₂ O ₈
h2oL	H ₂ O
anL	CaAl ₂ Si ₂ O ₈

1152 ΔG_i^{mod} terms are imposed on some end-members: $\Delta G_{\text{woL}}^{\text{mod}} = 1.3$ kJ, $\Delta G_{\text{silL}}^{\text{mod}} = -7.8$ kJ,

1153 $\Delta G_{\text{faL}}^{\text{mod}} = -8.2 - 1.4P$ kJ, and $\Delta G_{\text{foL}}^{\text{mod}} = -4$. The end-member anL is made by the reaction

1154 $\text{anL} = \text{woL} + \text{silL} + \Delta G_{\text{anL}}^{\text{od}}$, with $\Delta G_{\text{anL}}^{\text{od}} = -46.5 - 0.25P$.

1155 The composition of the melt is described by the following variables, where

1156 $\Sigma_c = \text{Si}_4\text{O}_8 + \text{NaAlSi}_3\text{O}_8 + \text{KAlSi}_3\text{O}_8 + \text{CaSiO}_3 + \text{Al}_2\text{SiO}_5 + \text{Fe}_4\text{Si}_2\text{O}_8 + \text{Mg}_4\text{Si}_2\text{O}_8 + \text{H}_2\text{O}$:

$$\begin{aligned}
 q &= \frac{\text{Si}_4\text{O}_8}{\Sigma_c} \\
 fsp &= \frac{\text{NaAlSi}_3\text{O}_8 + \text{KAlSi}_3\text{O}_8}{\Sigma_c} \\
 na &= \frac{\text{NaAlSi}_3\text{O}_8}{\text{NaAlSi}_3\text{O}_8 + \text{KAlSi}_3\text{O}_8} = \frac{\text{Na}}{\text{Na} + \text{K}} \\
 wo &= \frac{\text{CaSiO}_3}{\Sigma_c} \\
 sil &= \frac{\text{Al}_2\text{SiO}_5}{\Sigma_c} \\
 ol &= \frac{\text{Fe}_4\text{Si}_2\text{O}_8 + \text{Mg}_4\text{Si}_2\text{O}_8}{\Sigma_c} \\
 x &= \frac{\text{Fe}_4\text{Si}_2\text{O}_8}{\text{Fe}_4\text{Si}_2\text{O}_8 + \text{Mg}_4\text{Si}_2\text{O}_8} = \frac{\text{Fe}^{2+}}{\text{Fe}^{2+} + \text{Mg}}.
 \end{aligned}$$

1157 To handle the formation of the associate species anL, an ‘order parameter’ y_{anL} is defined,

1158 where $y_{\text{anL}} = p_{\text{anL}}$. The full set of end-member proportions can now be written as:

$$p_{\text{qL}} = q(1 + y_{\text{anL}})$$

$$p_{\text{abL}} = fsp \, na \, (1 + y_{\text{anL}})$$

$$p_{\text{kspL}} = f_{\text{sp}} (1 - na) (1 + y_{\text{anL}})$$

$$p_{\text{woL}} = wo (1 + y_{\text{anL}}) - y_{\text{anL}}$$

$$p_{\text{silL}} = sil (1 + y_{\text{anL}}) - y_{\text{anL}}$$

$$p_{\text{faL}} = ol x (1 + y_{\text{anL}})$$

$$p_{\text{foL}} = ol (1 - x) (1 + y_{\text{anL}})$$

$$p_{\text{h2oL}} = 1 - (q + f_{\text{sp}} + wo + sil + ol) (1 + y_{\text{anL}}) + y_{\text{anL}}$$

$$p_{\text{anL}} = y_{\text{anL}}$$

1159 The ubiquitous $(1 + y_{\text{anL}})$ terms arise because the reaction $\text{woL} + \text{silL} = \text{anL}$ leads to an
 1160 overall change in the number of ‘molecules’ present, for a fixed number of atoms of liquid.

1161 There are no site fractions in a formal sense since mixing is molecular. However it is
 1162 necessary to introduce an equivalent concept in order to formulate ideal activity
 1163 expressions. Considering melt as a one-phase site, the ‘site fractions’ are chosen to be
 1164 composed of the end-member proportion expressions p_{qL} , p_{woL} , p_{h2oL} , p_{anL} , $p_{\text{ol}} = p_{\text{faL}} + p_{\text{foL}}$,
 1165 $x_{\text{ab}} = p_{\text{abL}}$, $x_{\text{ksp}} = p_{\text{kspL}}$, and additionally the expressions

$$x_{\text{Fe}} = x$$

$$x_{\text{Mg}} = 1 - x$$

$$x_{\text{fac}} = 1 - p_{\text{h2oL}}$$

1166 The ideal activities are then written as follows, with the x_{Fe} and x_{Mg} terms allowing for an
 1167 extra entropic contribution from Fe-Mg mixing in addition to that of the mixing of foL and
 1168 faL units, and the x_{fac} term allowing for extra entropy in the addition of H_2O :

$$a_{\text{qL}}^{\text{ideal}} = x_{\text{fac}} p_{\text{qL}}$$

$$a_{\text{abL}}^{\text{ideal}} = x_{\text{fac}} x_{\text{ab}}$$

$$a_{\text{kspL}}^{\text{ideal}} = x_{\text{fac}} x_{\text{ksp}}$$

$$a_{\text{woL}}^{\text{ideal}} = x_{\text{fac}} p_{\text{woL}}$$

$$a_{\text{silL}}^{\text{ideal}} = x_{\text{fac}} p_{\text{silL}}$$

$$a_{\text{faL}}^{\text{ideal}} = x_{\text{fac}} p_{\text{ol}} (x_{\text{Fe}})^5$$

$$a_{\text{foL}}^{\text{ideal}} = x_{\text{fac}} p_{\text{ol}} (x_{\text{Mg}})^5$$

$$a_{\text{h2oL}}^{\text{ideal}} = (p_{\text{h2oL}})^2$$

$$a_{\text{anL}}^{\text{ideal}} = x_{\text{fac}} p_{\text{anL}}$$

1169 The non-ideal activities are given by equation (1). The symmetrical interaction energies are:

$W_{i,j}$ (kJ)	abL	kspL	woL	silL	faL	foL	h2oL	anL
qL	$12 - 0.4P$	$-2 - 0.5P$	-5	0	0	$42 + 1.0P$	$18.1 - 0.68P$	$-29.5 - 0.1P$
abL		$-6 + 3.0P$	-12.0	10	$-30 + 0.8P$	$-47.3 + 0.3P$	$-4.4 - 0.17P$	$8.6 + 0.4P$
kspL			-13	0	-11.3	6.8	$10.4 - 0.39P$	$-16 - 0.25P$
woL				-1.6	6.5	4	21	3.5
silL					12	12	$11 - 0.5P$	6.4
faL						18	29	$-43.5 - 0.95P$
foL							$29 - 0.5P$	$-26 - 0.6P$
h2oL								$9.75 - 0.5P$

1170 In version 6.3 of the Holland & Powell (2011) dataset, the thermodynamic properties of
1171 the h2oL end-member, incorporating the new constant-pressure heat capacity, are as
1172 follows. Enthalpy of formation ($\Delta_f H$): -281.68 ± 0.26 kJ, entropy (S): 66.60 kJ K⁻¹,
1173 volume (V): 1.363 J bar⁻¹, at 1 bar, 298 K. Heat capacity (C_P): 0.0650 kJ K⁻¹. Thermal
1174 expansivity (α_0): 57.80 K⁻¹. Bulk modulus at 1 bar, 298 K, and its first and second
1175 pressure derivatives ($\kappa_0, \kappa'_0, \kappa''_0$): 47.92 kbar, 4.00 , -0.08350 kbar⁻¹.

1176 Other models

1177 The a - x relations for biotite, garnet and orthopyroxene were first presented in White *et al.*
1178 (2014). As used in White *et al.* (2014), the a - x relations for epidote were taken from
1179 Holland & Powell (2011), those for feldspar from Holland & Powell (2003), and those for
1180 spinel-magnetite from White *et al.* (2002). For ilmenite, the Mg-bearing model used by

1181 White *et al.* (2014) has been replaced, in both the metabasite set and the metapelite set,
1182 with the older model of White *et al.* (2000) in the system FeO–Fe₂O₃–TiO₂, as the more
1183 recent model appears to predict excessive values of MgO/(FeO+MgO) in the phase.

Author Manuscript

1184 **FIGURE CAPTIONS**

1185 Figure 1: Comparison of model calculations with experiments in the pyroxene
1186 quadrilateral, diopside (di) – enstatite (en) – ferrosilite (fs) – hedenbergite (hed).
1187 (a)–(d) The quadrilateral itself, displaying the data of Turnock & Lindsley (1981) and
1188 Lindsley (1983) in black. Black arrowheads show the directions of approach to
1189 equilibrium compositions; black lines are tielines defining the miscibility gap and
1190 solvus. Grey curves and lines indicate the calculated miscibility limits; dashed grey
1191 curves show the metastable extension of the augite–pigeonite solvus within the
1192 augite–orthopyroxene miscibility gap. (e)–(f) The fs–hed binary subsystem, displaying
1193 the experimental brackets of Lindsley (1981). Fs_{ss} and hed_{ss} are solid solutions rich in
1194 the fs and hed end-members respectively.

1195 Figure 2: Pseudosections calculated using the metabasite set of thermodynamic models for
1196 an oxidised MORB bulk composition, based on that of Sun & McDonough (1989) but
1197 with a greater M_O , giving $X_{Fe^{3+}}=0.36$ (SM89, Table 1). Panels (a), (b): calculations
1198 using the augite model for clinopyroxene. Panels (c), (d): correctly modelled using the
1199 omphacite model for clinopyroxene. Where clinopyroxene is truly augitic in
1200 composition, the two models are substantially consistent, but the augite model is
1201 unable to represent moderate to high Na contents or the coexisting clinopyroxene
1202 phases highlighted in (b) and (d). H_2O was taken to be in excess below the solidus;
1203 above the solidus values of 5.8 mole % were used for (a), (b) and 5.6 mole % for (c),
1204 (d), such that assemblages are just H_2O -saturated at the solidus. Removal of K_2O ,
1205 TiO_2 from the amphibole model has negligible effect on phase boundaries. The bulk
1206 composition is the same as in Diener & Powell (2012), fig. 1c, which was calculated
1207 with the previous generation of models.

1208 Figure 3: Pseudosections calculated with the metabasite set for the SQA composition of
1209 Patiño Douce & Beard (1995) (Table 1). (a) P – T pseudosection compared with

1210 experiments. Experimental assemblages are q + pl + ilm/ru ± hb ± opx ± cpx ± g ±
1211 L. Two different M_O values are used at higher and lower pressure, corresponding to
1212 different sets of experimental apparatus (see text). (b) Summary of (a) highlighting
1213 the implied facies transition. (c) T - M_O section at 7 kbar, representing values of $X_{Fe^{3+}}$
1214 ≤ 0.5 . (d) T - M_{H_2O} sections at 7 kbar. (e) Melt fraction as a function of T at 7 kbar;
1215 melt fraction is molar with phases represented on a 1-cation basis, approximating the
1216 volumetric melt fraction. Boundaries are ornamented and coloured to highlight the
1217 continuation of phase-out curves through different assemblages (colour online).

1218 Figure 4: Pseudosections calculated with the metabasite set for sample 478 of Beard &
1219 Lofgren (1991; BL478 in Table 1). (a) P - T pseudosection compared with
1220 experiments. Experimental assemblages are pl + mt + ilm ± hb ± opx ± cpx ± q.
1221 The experiments involved hydrate-breakdown melting except for one, marked with a
1222 square symbol, which was fluid-saturated. (b) Summary of (a) highlighting the
1223 implied facies transition. (c) T - M_O section at 7 kbar, representing values of $X_{Fe^{3+}} \leq$
1224 0.5. (d) T - M_{H_2O} sections at 7 kbar. Boundaries are ornamented and coloured to
1225 highlight the continuation of phase-out curves through different assemblages (colour
1226 online). In calculating this figure, the clinoamphibole model was used with $\Delta G_{gl}^{mod}=0$
1227 kJ, rather than the preferred value of -3 kJ; however this affects the position of phase
1228 field boundaries by $\leq 10^\circ\text{C}$.

1229 Figure 5: Interpreted temperature of the hornblende-out boundary in six experimental
1230 bulk compositions (brackets and half-brackets labelled with assemblages; bulk
1231 compositions in Table 1), compared with the temperatures obtained from calculations
1232 using a range of M_O and M_{H_2O} values (blue bars, colour online). Except in the case of
1233 compositions labelled a , calculations were performed for a range of M_O such that 0.1
1234 $< X_{Fe^{3+}} < 0.25$, and for $3.5 < M_{H_2O} < 6.5$ mole% (~ 1 - 2 wt% H_2O), varied
1235 simultaneously. For compositions a , the blue bars represent calculations for the

1236 restricted range of M_{O} or $M_{\text{H}_2\text{O}}$ over which positive modes of phases were predicted
1237 (Table 1). For composition WW94, TiO_2 was omitted as hornblende is the only
1238 Ti-bearing model involved. In compositions b , only trace hornblende was detected at
1239 the lower- T end of the experimental bracket. Calculations were made on each
1240 experimental assemblage without checking that it was the most stable assemblage that
1241 the models could generate, except for compositions c , which were used in calibration.
1242 For BL478, the experimental assemblage is ambiguous, while in the calculations,
1243 stable assemblages \pm quartz are needed to cover the full range of M_{O} and $M_{\text{H}_2\text{O}}$.

Author Manuscript

1244 **TABLE CAPTIONS**

1245 Table 1: Bulk compositions in mole % used in calculations, expressed in terms of the
 1246 chemical components used by THERMOCALC. FeO^{tot} is total iron expressed as FeO. O,
 1247 oxygen, combines only with FeO, via the equation $2 \text{FeO} + \text{O} = \text{Fe}_2\text{O}_3$; hence M_{O} is
 1248 identically equal to molar bulk Fe_2O_3 , $M_{\text{Fe}_2\text{O}_3}$, with $X_{\text{Fe}^{3+}}$ given by $2 M_{\text{O}}/M_{\text{FeO}^{\text{tot}}}$.
 1249 Where no value is cited in the $M_{\text{H}_2\text{O}}$ column, H_2O is assumed to be in excess.

1250 Table 2: Equilibria used in calibrating the augite model (see text), and results of
 1251 calculations with the completed set of models. Observed values of compositional
 1252 variables are shown in roman font, calculated values in italic. Compositional variables
 1253 for the augite model are defined in the Appendix. Bulk compositions used in the
 1254 calculations are given in Table 1. Observational $f(\text{aug})$ values ($x_{\text{Fe}_3}^{\text{M1}}$) obtained using
 1255 the rule of Droop (1987).

1256 Table 3: Equilibria used in calibrating the clinoamphibole model, and the results of
 1257 calculations with the completed set of models (all with excess q, H_2O). Observed or
 1258 other target values (see footnotes) of compositional variables are shown in roman font,
 1259 calculated values in italics. Compositional variables for the clinoamphibole and augite
 1260 models are defined in the Appendix. Bulk compositions used in the calculations are
 1261 given in Table 1. $\text{Phase} \rightarrow 0$ indicates the zero-mode isopleth (the *phase-out*
 1262 boundary) for *phase*.

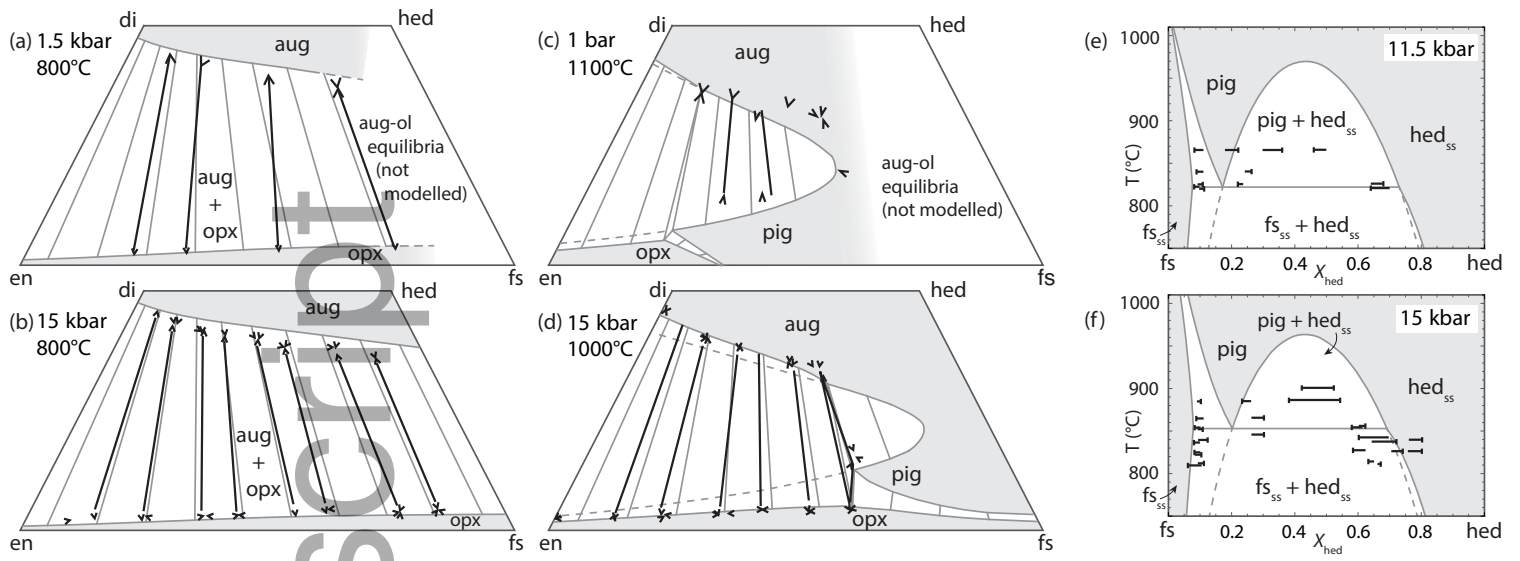
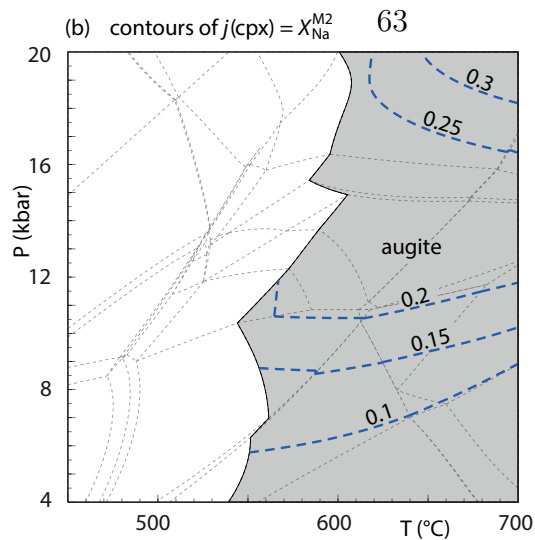
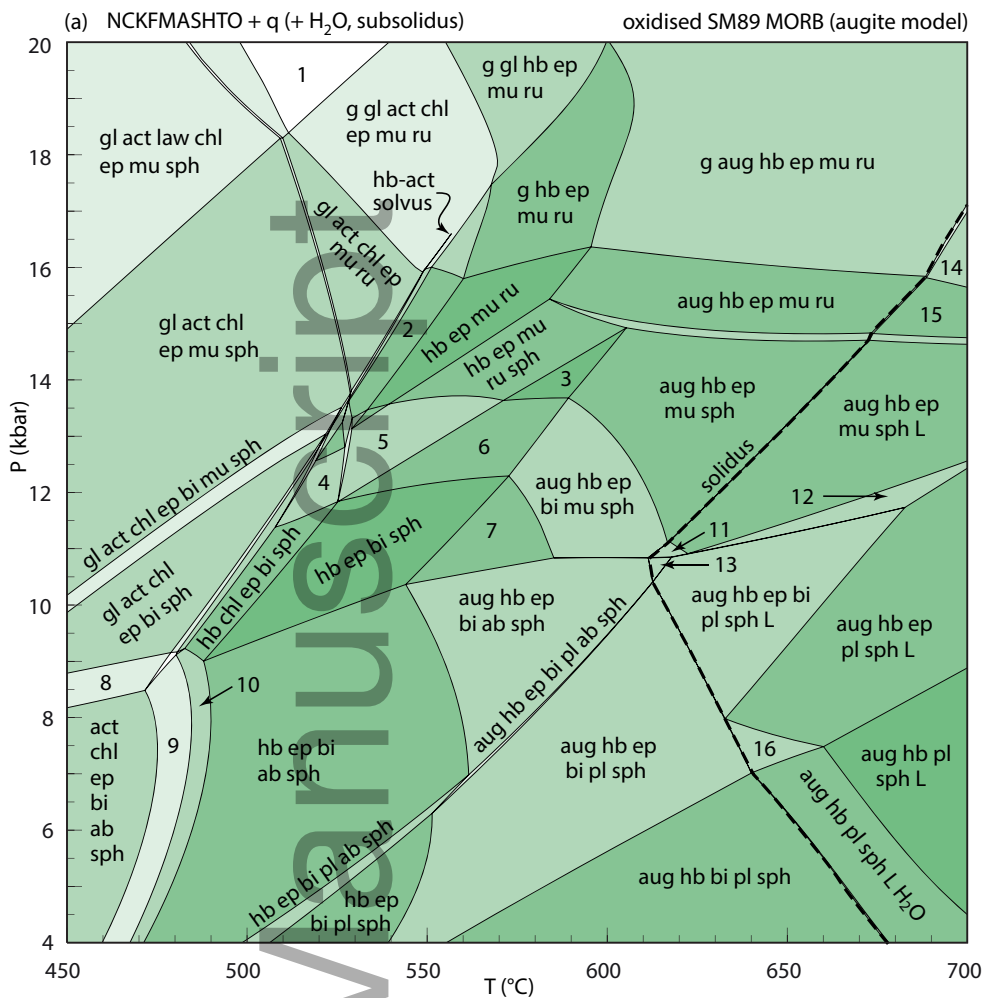
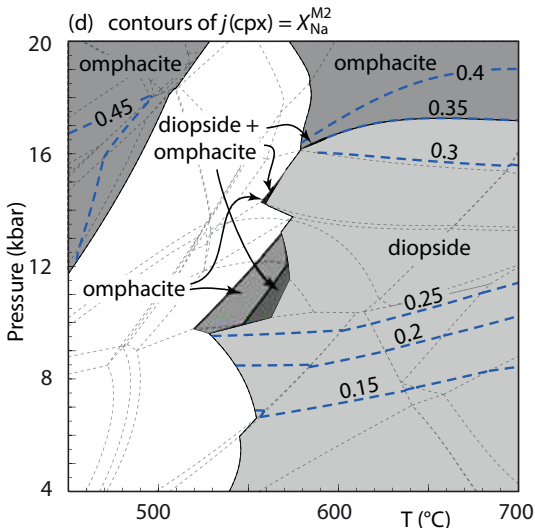
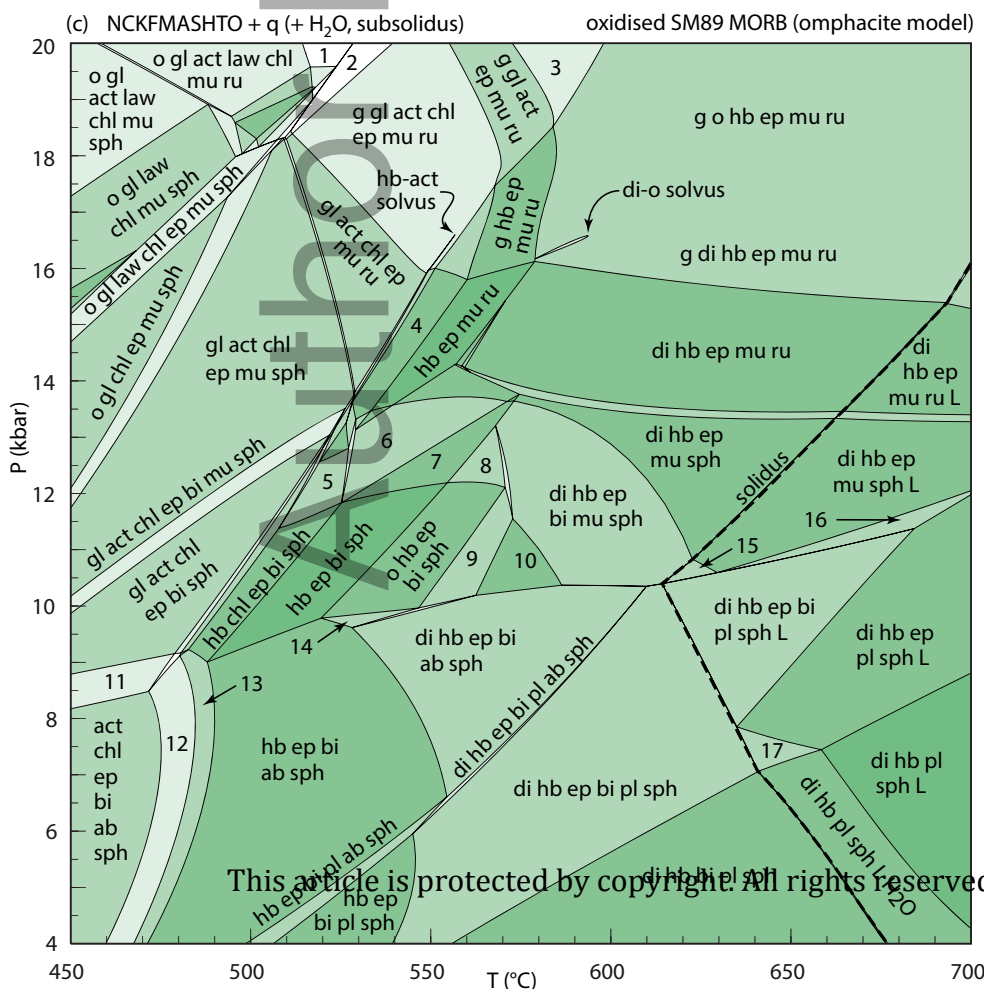


Figure 1:



- 1) g gl act law chl ep mu ru
- 2) hb chl ep mu ru
- 3) hb ep mu sph
- 4) hb chl ep bi mu sph
- 5) hb ep mu bi ru sph
- 6) hb ep bi mu sph
- 7) aug hb ep bi sph
- 8) gl act chl ep bi ab sph
- 9) hb act chl ep bi ab sph
- 10) hb chl ep bi ab sph
- 11) aug hb ep bi mu sph L
- 12) aug hb ep mu pl sph L
- 13) aug hb ep bi ab sph L
- 14) g aug hb ep mu ru L
- 15) aug hb ep mu ru L
- 16) aug hb ep pl sph L H₂O



- 1) g o gl act law chl mu ru
- 2) g gl act law chl ep mu ru
- 3) g o gl act ep mu ru
- 4) hb chl ep mu ru
- 5) hb chl ep mu bi sph
- 6) hb ep mu bi ru sph
- 7) hb ep mu bi sph
- 8) o hb ep mu bi sph
- 9) o di hb ep bi sph
- 10) di hb ep bi sph
- 11) gl act chl ep bi ab sph
- 12) hb act chl ep bi ab sph
- 13) hb chl ep bi ab sph
- 14) o hb ep bi ab sph
- 15) di hb ep bi mu sph L
- 16) di hb ep mu pl sph L
- 17) di hb ep pl sph L H₂O

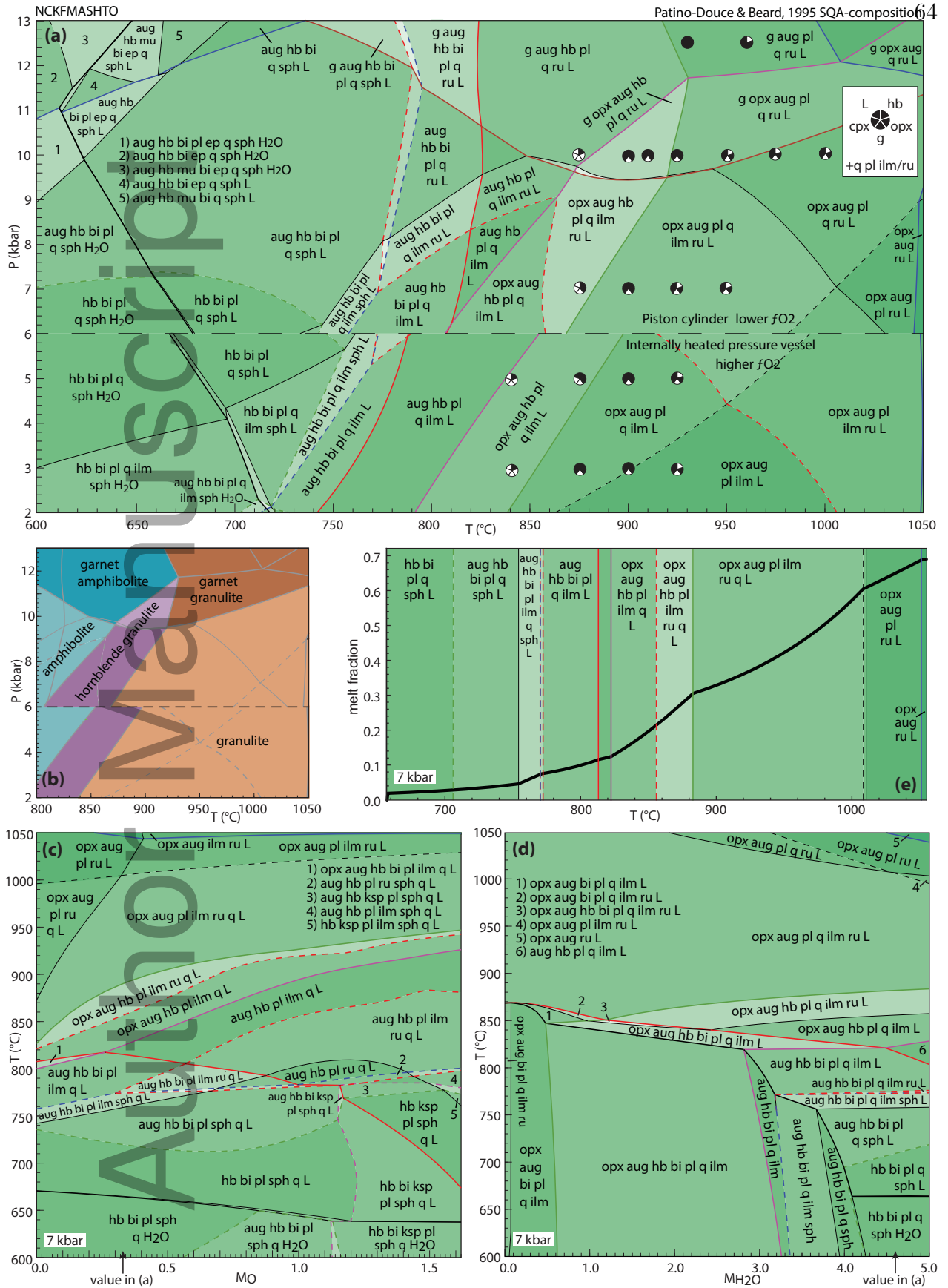


Figure 3:

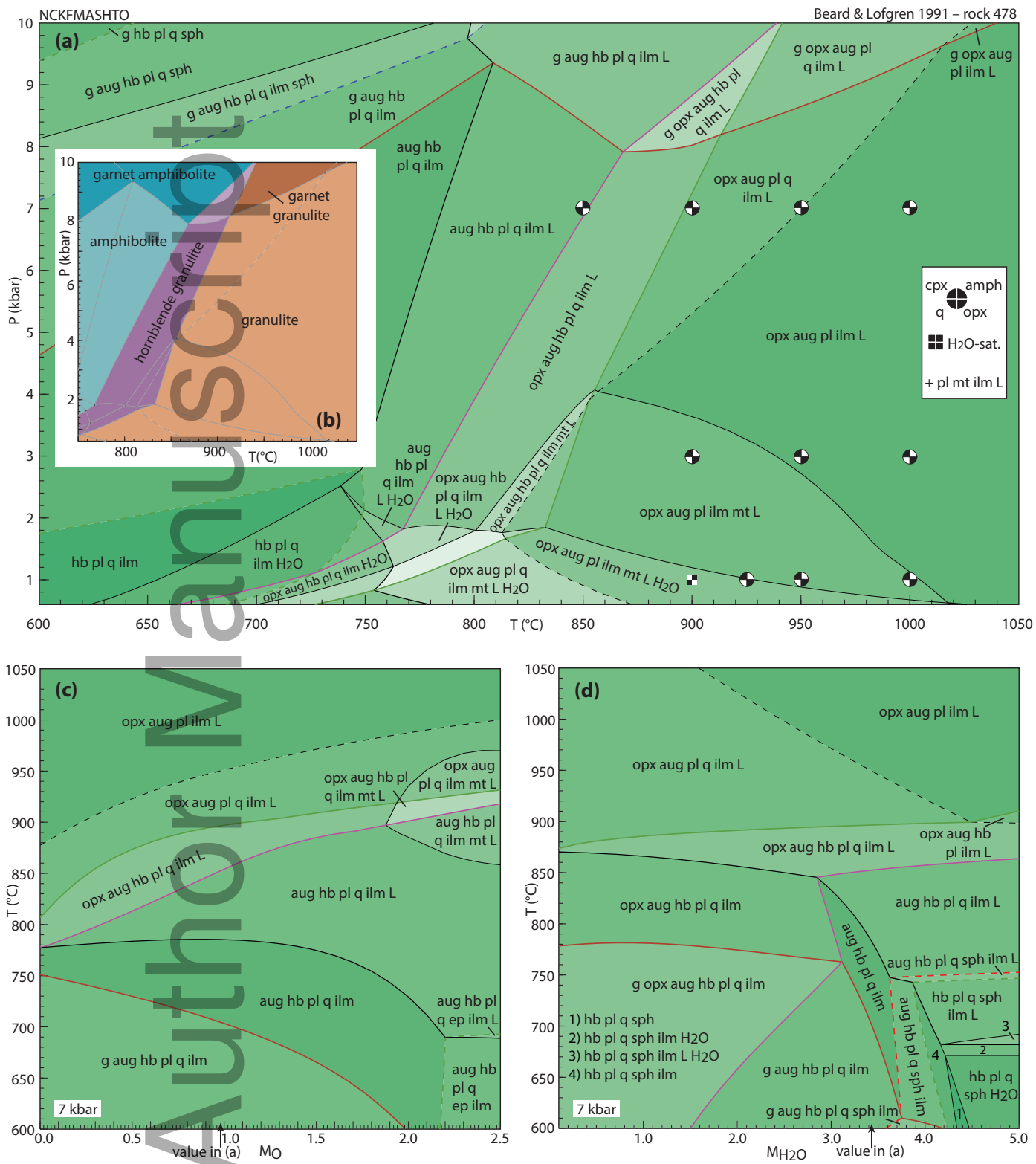


Figure 4:

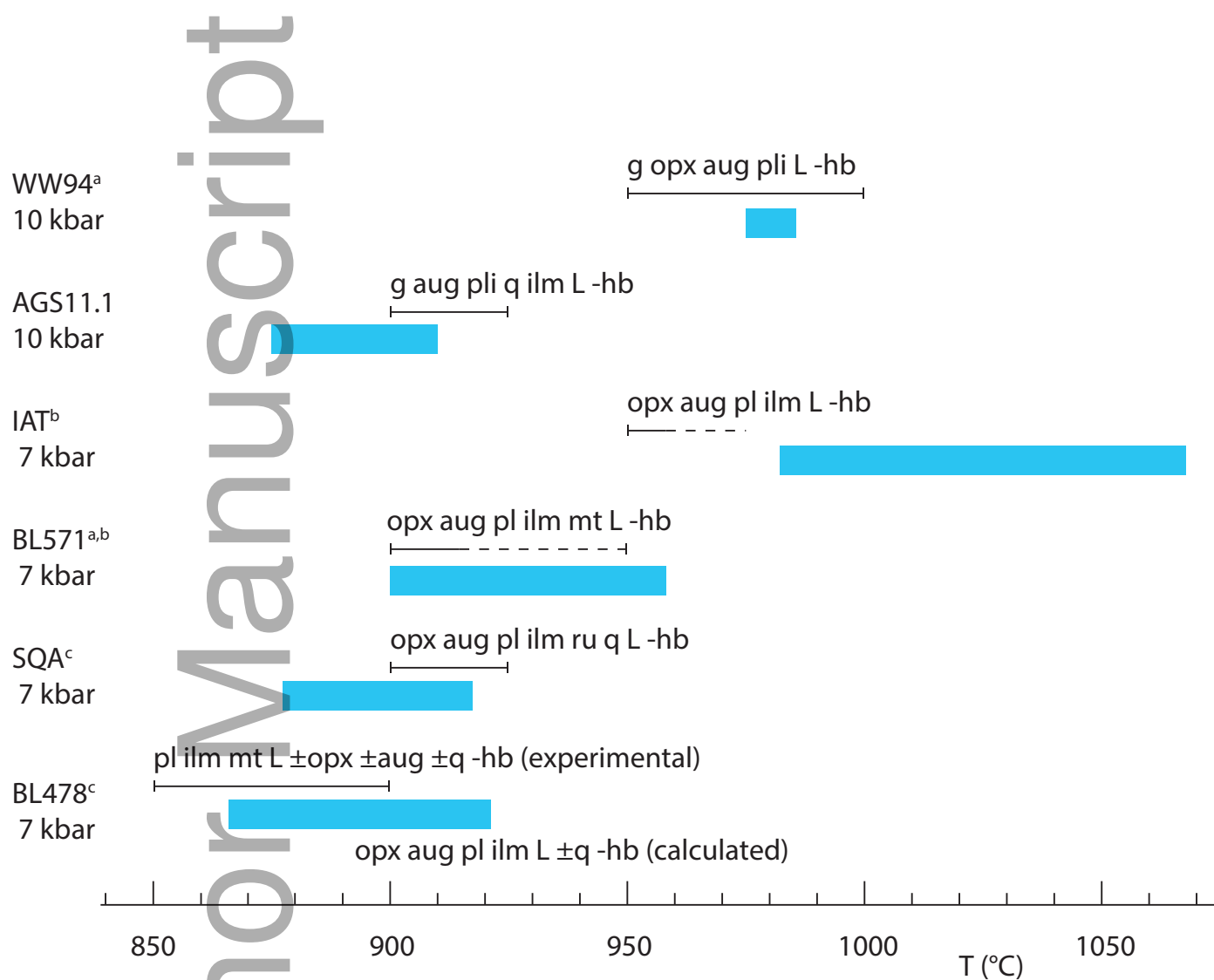


Table 1:

	M_{SiO_2}	M_{TiO_2}	$M_{\text{Al}_2\text{O}_3}$	$M_{\text{FeO}^{\text{tot}}}$	M_{MgO}	M_{CaO}	$M_{\text{Na}_2\text{O}}$	$M_{\text{K}_2\text{O}}$	M_{O}	$M_{\text{H}_2\text{O}}$
Mcal	55.21	1.01	8.75	7.84	12.22	11.75	2.51	0.22	0.47	
SM89	52.47	1.05	9.10	8.15	12.71	12.21	2.61	0.23	1.47	
IZ100	52.05	1.29	13.24	10.18	7.70	12.14	2.89		0.51	
dP0669	58.29	0.99	11.55	6.45	7.18	8.97	4.59	1.14	0.84	
DR9734	47.05	0.18	8.77	5.43	19.02	17.52	1.39	0.04	0.60	
SKA101	58.26	1.42	9.15	11.98	8.80	8.61	0.49	0.70	0.60	
SKB116	53.72	1.75	9.10	12.40	7.43	10.85	2.95	0.42	1.38	
PM13013	52.95	1.70	8.42	11.61	9.86	11.22	2.72	0.62	0.89	
PM13083	53.24	0.83	8.62	9.71	11.32	12.48	2.41	0.19	1.19	
PM13161	53.13	1.08	8.01	9.05	11.71	12.31	3.14	0.43	1.15	
AG9	51.08	1.37	9.68	11.66	11.21	13.26	0.79	0.16	0.80	
SQA (high- P)	60.05	1.27	6.62	6.57	9.93	8.31	1.83	0.44	0.33	4.64
SQA (low- P)	59.76	1.26	6.59	6.54	9.88	8.27	1.82	0.44	0.81	4.62
BL478	53.96	1.35	9.26	10.14	8.11	10.15	2.54	0.11	0.98	3.42
WW94	50.09	0.31	8.91	7.27	16.50	15.86	1.00	0.07	0.35–0.86	3.50–5.00
AGS11.1	58.31	0.75	8.62	10.90	8.44	11.44	1.14	0.41	0.52–1.30	3.50–6.50
IAT	55.99	0.81	10.41	6.90	12.12	10.33	3.24	0.18	0.33–0.82	3.50–6.50
BL571	56.03	1.28	10.17	11.15	7.18	10.46	3.49	0.26	1.20–1.30	3.50–6.50

Mcal: MORB-like composition used in calibration. **SM89**: oxidised average MORB composition of Sun & McDonough (1989) (the analysed composition has $M_{\text{O}}=0.5$ mole %). **IZ100**: natural metabasite sample of Kunz *et al.* (2014), M_{O} estimate from pseudosection modelling. **dP0669**: Breaksea Orthogneiss sample 0669 (dioritic gneiss), De Paoli (2006), M_{O} from wet chemistry. **DR9734**: microprobe analysis of experimental glass, ground from a garnet pyroxenite xenolith, by Adam *et al.* (1992); M_{O} was assumed for the current study. **SKA101**, **SKB116**, **PM13013**, **PM13083**, **PM13161**, **AG9**: Natural amphibolites and low-temperature granulites (unpublished), $X_{\text{Fe}^{3+}}$ estimated at 0.10–0.25 from previous pseudosection modelling. **SQA**: Synthetic amphibolite composition of Patiño Douce & Beard (1995) (glass analysis). The compositions at high and low P are the same except for different assumed M_{O} values at high- P (piston cylinder apparatus) and low- P (internally heated pressure vessel); see text. $M_{\text{H}_2\text{O}}$ from analysis of starting material. In Fig. 5, $0.33 < M_{\text{O}} < 0.82$, $3.50 < M_{\text{H}_2\text{O}} < 6.50$. **BL478**: Sample 478 of Beard & Lofgren (1991). See text for $M_{\text{H}_2\text{O}}$, M_{O} estimates. In Fig. 5, $0.52 < M_{\text{O}} < 1.30$, $3.50 < M_{\text{H}_2\text{O}} < 6.50$. **WW94**: natural amphibolite composition of Wolf & Wyllie (1994). **AGS11.1**: natural amphibolite composition of Skjerlie & Patiño Douce (1995). **IAT**: meta island arc tholeiite of Rushmer (1991). **BL571**: Sample 571 of Beard & Lofgren (1991).

Table 2:

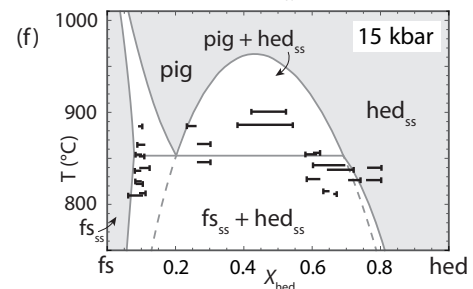
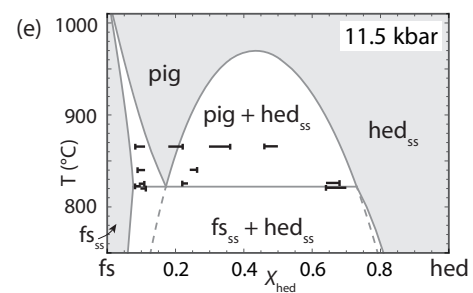
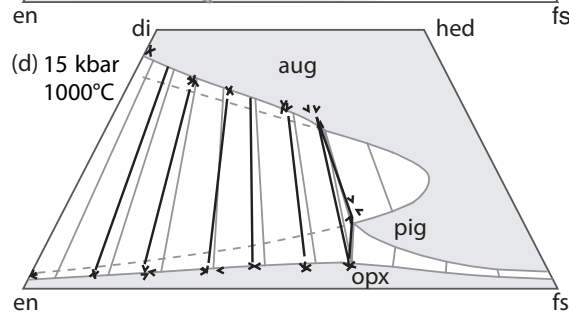
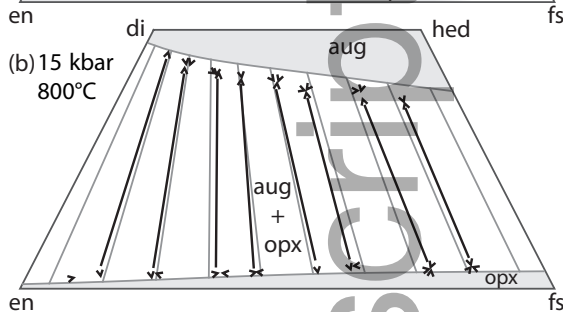
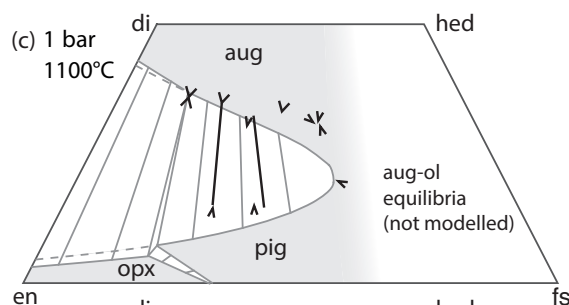
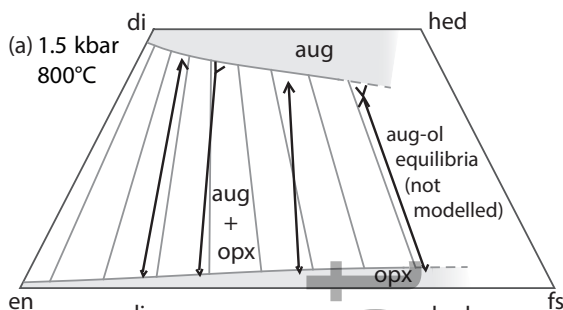
	Assemblage	P (kbar)	T ($^{\circ}\text{C}$)	$x(\text{aug})$	$y(\text{aug})$	$f(\text{aug})$	$z(\text{aug})$	$j(\text{aug})$	$x_{\text{Ca}}^{\text{X}}(g)$	$x^{\text{an}}(pl)$
IZ100 ¹	cpx opx g pl ilm	9	900	0.26	0.08	0.06	0.89	0.04	0.19	0.53
				<i>0.34</i>	<i>0.06</i>	<i>0.07</i>	<i>0.81</i>	<i>0.05</i>	<i>0.20</i>	<i>0.56</i>
dP0669 ²	cpx opx g pl bi ilm q H ₂ O	11	880	0.25	0.10	0.05	0.80	0.05	0.20	0.50
				<i>0.25</i>	<i>0.01</i>	<i>0.11</i>	<i>0.73</i>	<i>0.15</i>	<i>0.20</i>	<i>0.31</i>
1303/DR9734 ³	cpx g pl sp	10	1000	0.17	0.19	0.03	0.77	0.07	0.21	0.64
				<i>0.14</i>	<i>0.09</i>	<i>0.06</i>	<i>0.81</i>	<i>0.06</i>	<i>0.18</i>	<i>0.57</i>

¹Natural sample (Kunz *et al.*, 2014). P - T estimate from pseudosection forward modelling of intercalated metapelitic rocks using the ds55 models. ²Natural sample from De Paoli (2006). P - T estimate from the author's pseudosection forward modelling using the ds55 models. Representative values of compositional variables given to nearest 0.05. ³Experimental run 1303 of Adam *et al.* (1992), with starting material DR9734.

Table 3:

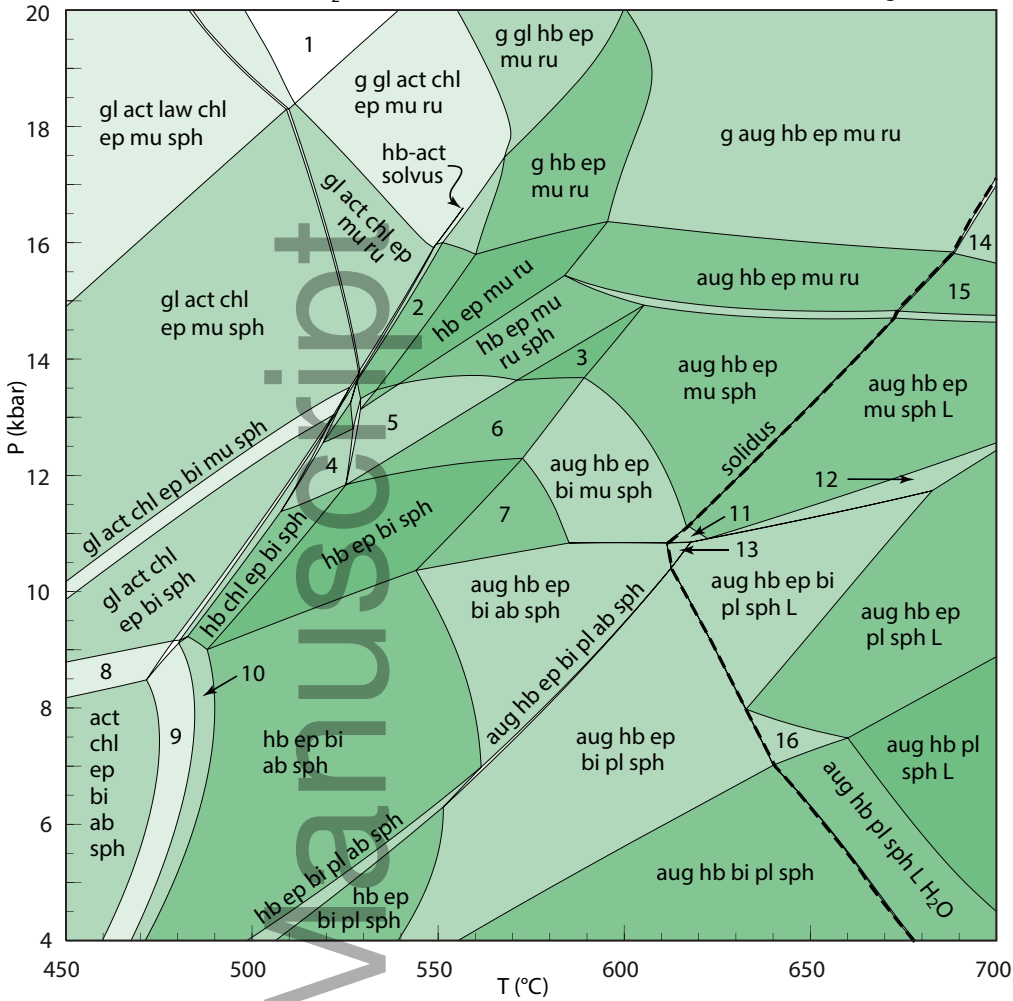
Assemblage		P (kbar)	T (°C)	Composition variables									
Mcal ¹	hb gl act bi ep chl	10±1	480±20	<i>y</i> (hb)	<i>z</i> (hb)	<i>a</i> (hb)	<i>c</i> (hb)	<i>f</i> (hb)	<i>y</i> (gl)	<i>z</i> (gl)	<i>a</i> (gl)	<i>c</i> (gl)	<i>f</i> (gl)
	ab sph;	<i>9.3</i>	<i>474</i>	<i>0.55–0.70</i>	<i>0.3–0.4</i>	<i>0.35–0.45</i>	<i>0.6–0.7</i>	<i>0.1</i>	<i>0.7–0.8</i>	<i>0.8–0.9</i>	<i>0.1</i>	<i>0.1</i>	<i>0.1</i>
	hb, gl→0			<i>0.63</i>	<i>0.38</i>	<i>0.37</i>	<i>0.61</i>	<i>0.08</i>	<i>0.78</i>	<i>0.89</i>	<i>0.07</i>	<i>0.11</i>	<i>0.09</i>
				<i>y</i> (act)	<i>z</i> (act)	<i>a</i> (act)	<i>c</i> (act)	<i>f</i> (act)					
				<i>0.15–0.25</i>	<i>0.15–0.25</i>	<i>0.1</i>	<i>0.75–0.80</i>	<i>0.05</i>					
				<i>0.17</i>	<i>0.22</i>	<i>0.07</i>	<i>0.78</i>	<i>0.03</i>					
SKA101 ²	hb g pl bi ilm sph	10	770	<i>a</i> (hb)	<i>k</i> (hb)	<i>t</i> (hb)	<i>y</i> (aug)	<i>z</i> (aug)	<i>j</i> (aug)	<i>x</i> _{Ca} ^X (g)	<i>x</i> ^{an} (pl)		
				<i>0.41</i>	<i>0.31</i>	<i>0.08</i>	-	-	-	<i>0.27</i>	<i>0.86</i>		
SKB116 ²	hb cpx g pl bi sph	11	770	<i>0.65</i>	<i>0.34</i>	<i>0.07</i>				<i>0.28</i>	<i>0.83</i>		
				<i>0.56</i>	<i>0.38</i>	<i>0.12</i>	<i>0.03</i>	<i>0.87</i>	<i>0.02</i>	<i>0.30</i>	<i>0.47</i>		
PM13013 ²	hb pl ilm	4	700	<i>0.72</i>	<i>0.16</i>	<i>0.07</i>	<i>0.09</i>	<i>0.86</i>	<i>0.11</i>	<i>0.43</i>	<i>0.26</i>		
				<i>0.71</i>	<i>0.31</i>	<i>0.11</i>	-	-	-	-	<i>0.36</i>		
PM13083 ²	hb cpx pl sph	4	700	<i>0.39</i>	<i>0.35</i>	<i>0.05</i>					<i>0.38</i>		
				<i>0.44</i>	<i>0.11</i>	<i>0.07</i>	<i>0.07</i>	<i>0.93</i>	<i>0.04</i>	-	<i>0.51</i>		
PM13161 ^{2,3}	hb cpx pl sph	4	700	<i>0.51</i>	<i>0.14</i>	<i>0.05</i>	<i>0.06</i>	<i>0.92</i>	<i>0.04</i>		<i>0.49</i>		
				<i>0.65</i>	<i>0.18</i>	<i>0.07</i>	<i>0.08</i>	<i>0.52</i>	<i>0.02</i>	-	<i>0.26</i>		
AG9 ⁴	hb g pl ilm; g→0	6±3	650	<i>0.49</i>	<i>0.19</i>	<i>0.04</i>	<i>0.02</i>	<i>0.89</i>	<i>0.08</i>		<i>0.29</i>		
				<i>0.29</i>	<i>0.17</i>	<i>0.04</i>	-	-	-	<i>0.96</i>			
				<i>0.32</i>	<i>0.19</i>	<i>0.04</i>				<i>0.47</i>	<i>0.95</i>		

¹Hb, gl, act were assumed to have negligible K₂O, TiO₂, with $k(\text{hb}) > k(\text{gl}) \approx k(\text{act})$ and $t(\text{hb}) \approx t(\text{gl}) > t(\text{act})$; calculated values are $0.02 < k < 0.04$, $t \leq 0.01$, with appropriate differences among the three phases. ² P - T estimated from pseudosection forward modelling with ds55 models. ³Measured $j(\text{aug})$ looks suspect. ⁴Garnet has 20% spessartine, unmodelled.

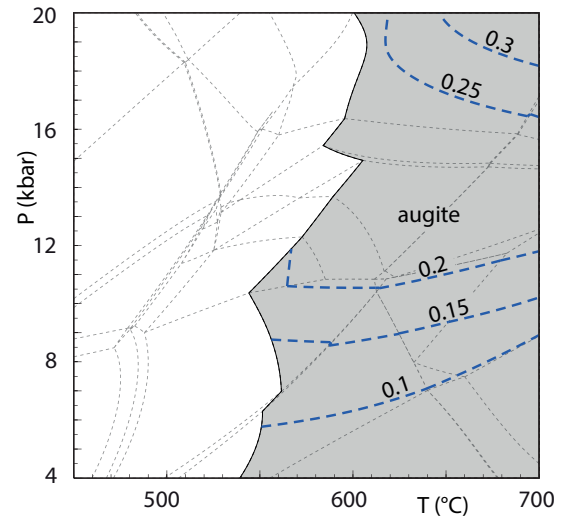


jmg_12211_f1.eps

(a) NCKFMASHTO + q (+ H₂O, subsolidus) oxidised SM89 MORB (augite model)

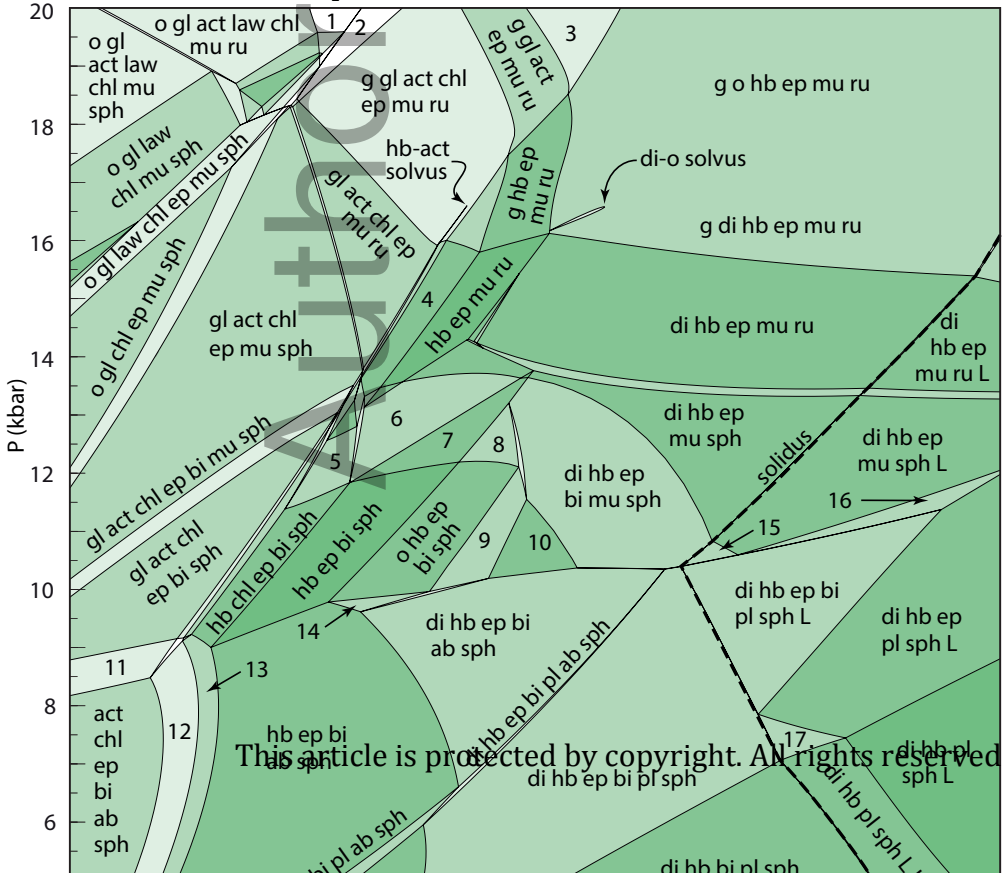


(b) contours of $j(\text{cpx}) = X_{\text{Na}}^{\text{M2}}$

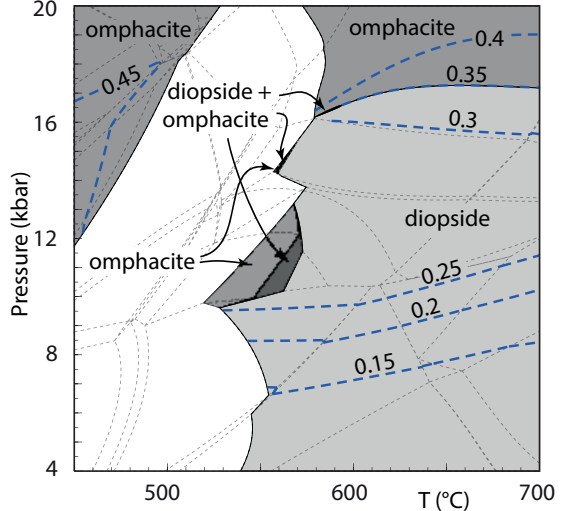


- 1) g gl act law chl ep mu ru
- 2) hb chl ep mu ru
- 3) hb ep mu sph
- 4) hb chl ep bi mu sph
- 5) hb ep mu bi ru sph
- 6) hb ep bi mu sph
- 7) aug hb ep bi sph
- 8) gl act chl ep bi ab sph
- 9) hb act chl ep bi ab sph
- 10) hb chl ep bi ab sph
- 11) aug hb ep bi mu sph L
- 12) aug hb ep mu pl sph L
- 13) aug hb ep bi ab sph L
- 14) g aug hb ep mu ru L
- 15) aug hb ep mu ru L
- 16) aug hb ep pl sph L H₂O

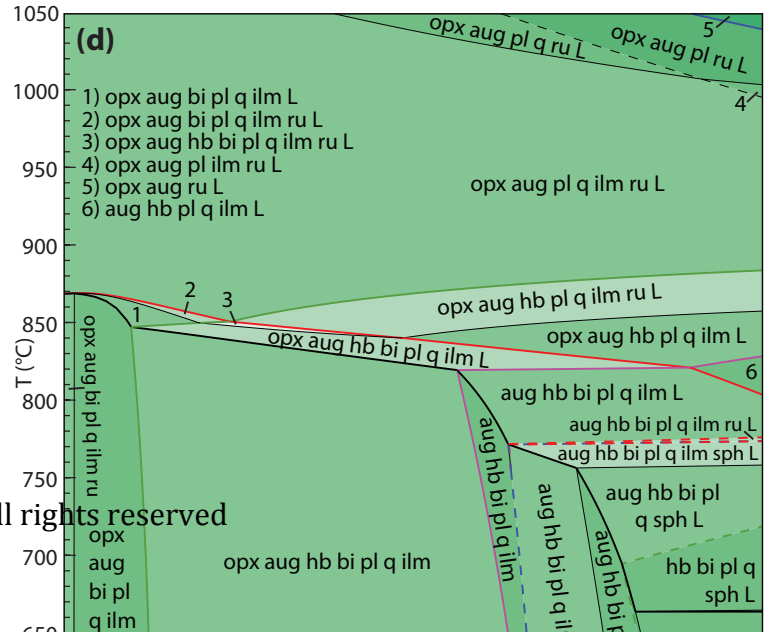
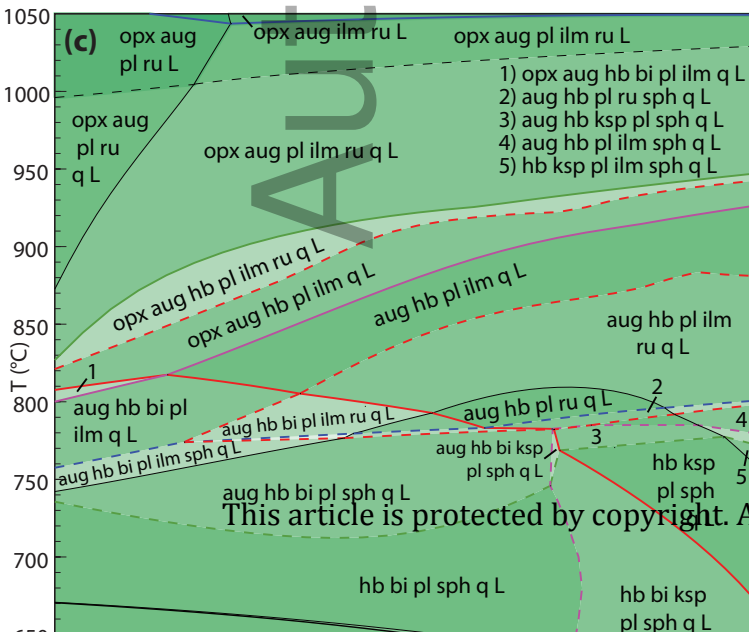
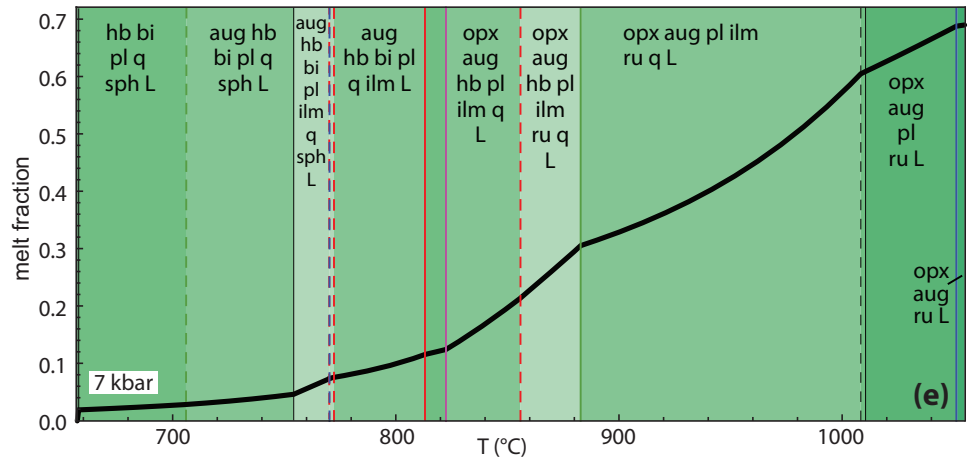
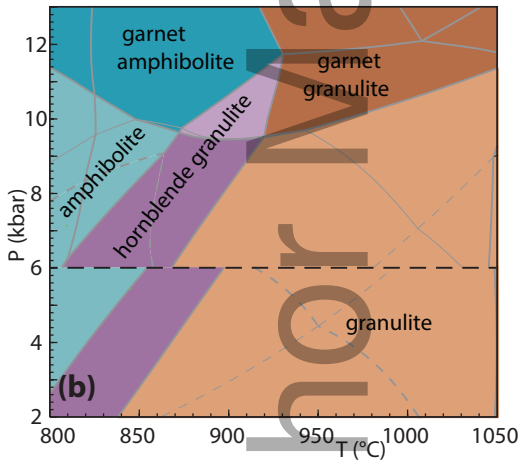
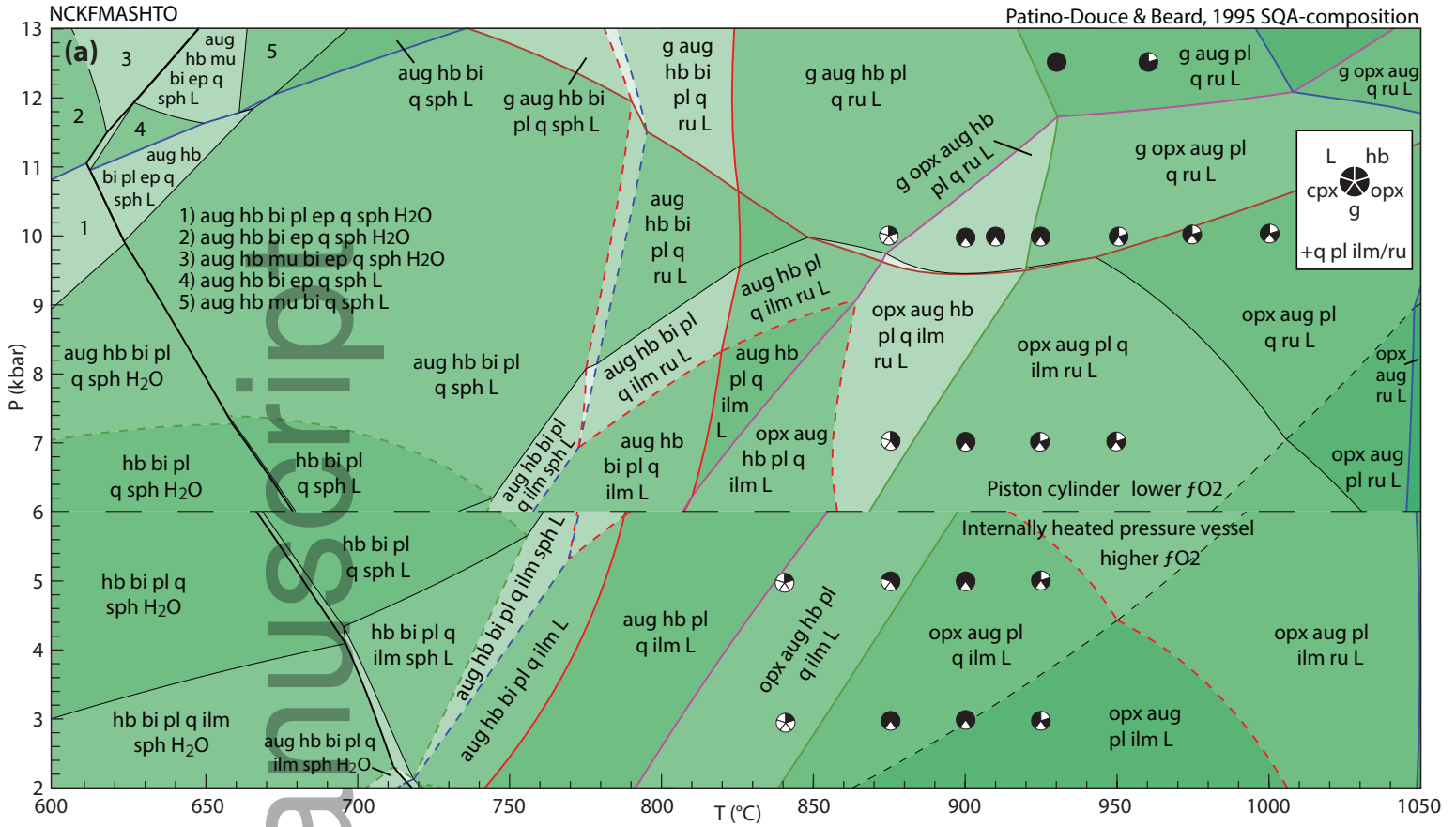
(c) NCKFMASHTO + q (+ H₂O, subsolidus) oxidised SM89 MORB (omphacite model)



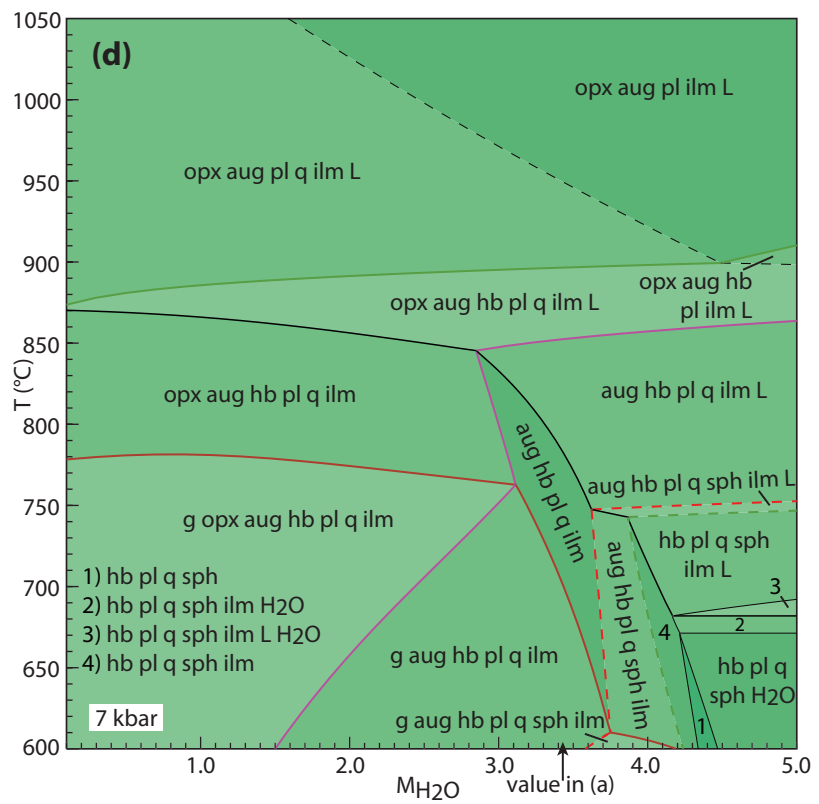
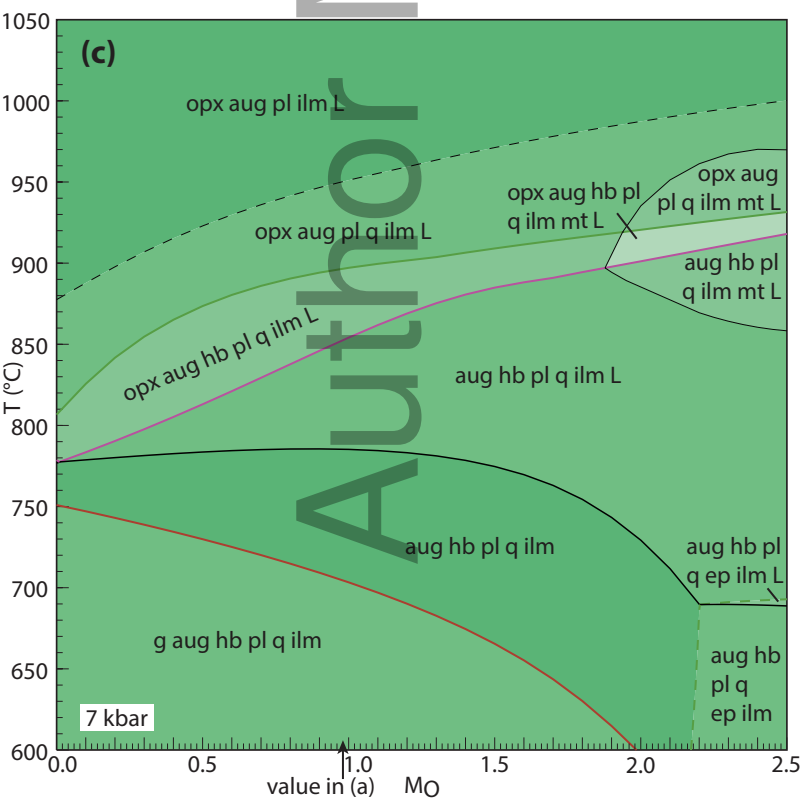
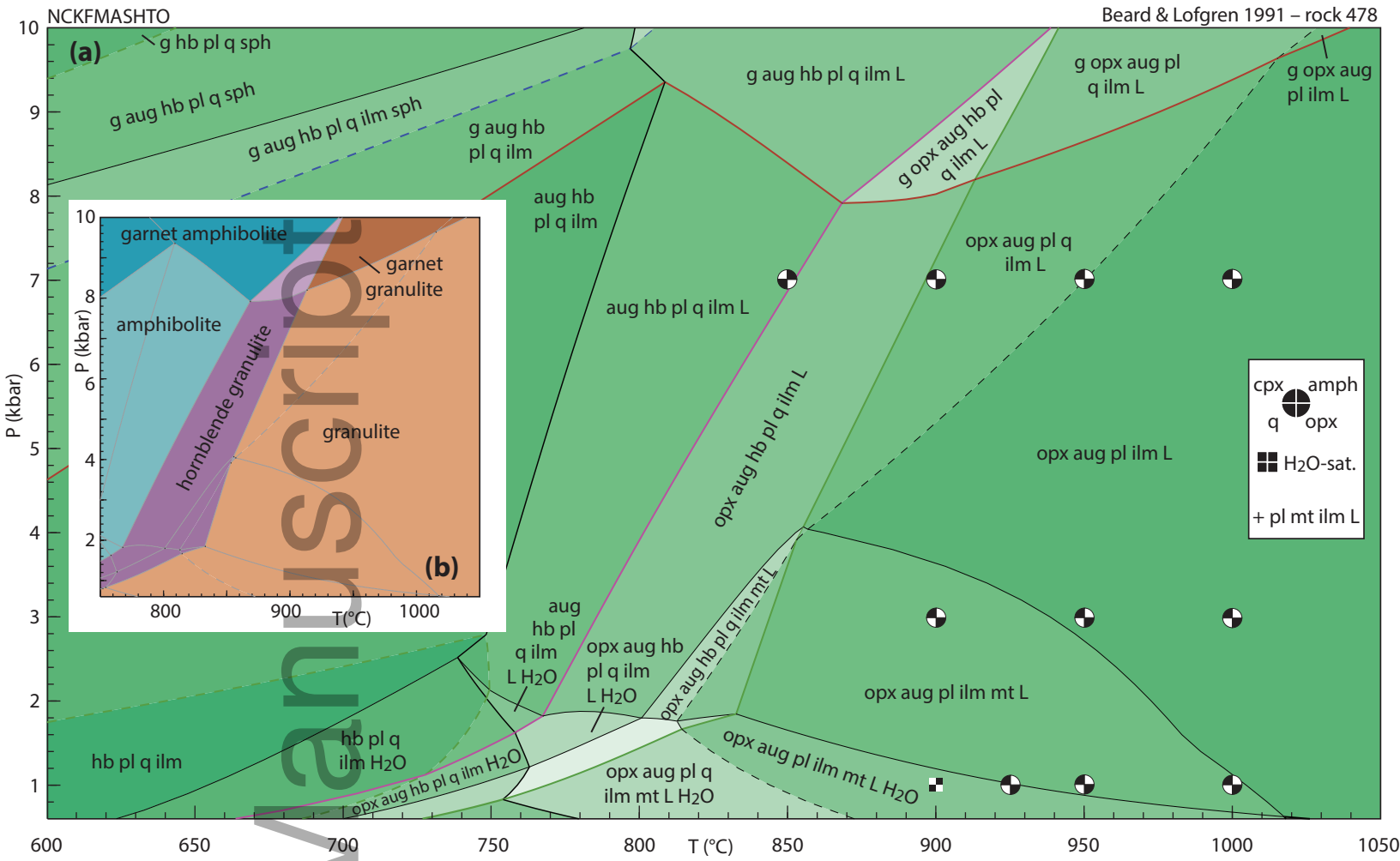
(d) contours of $j(\text{cpx}) = X_{\text{Na}}^{\text{M2}}$

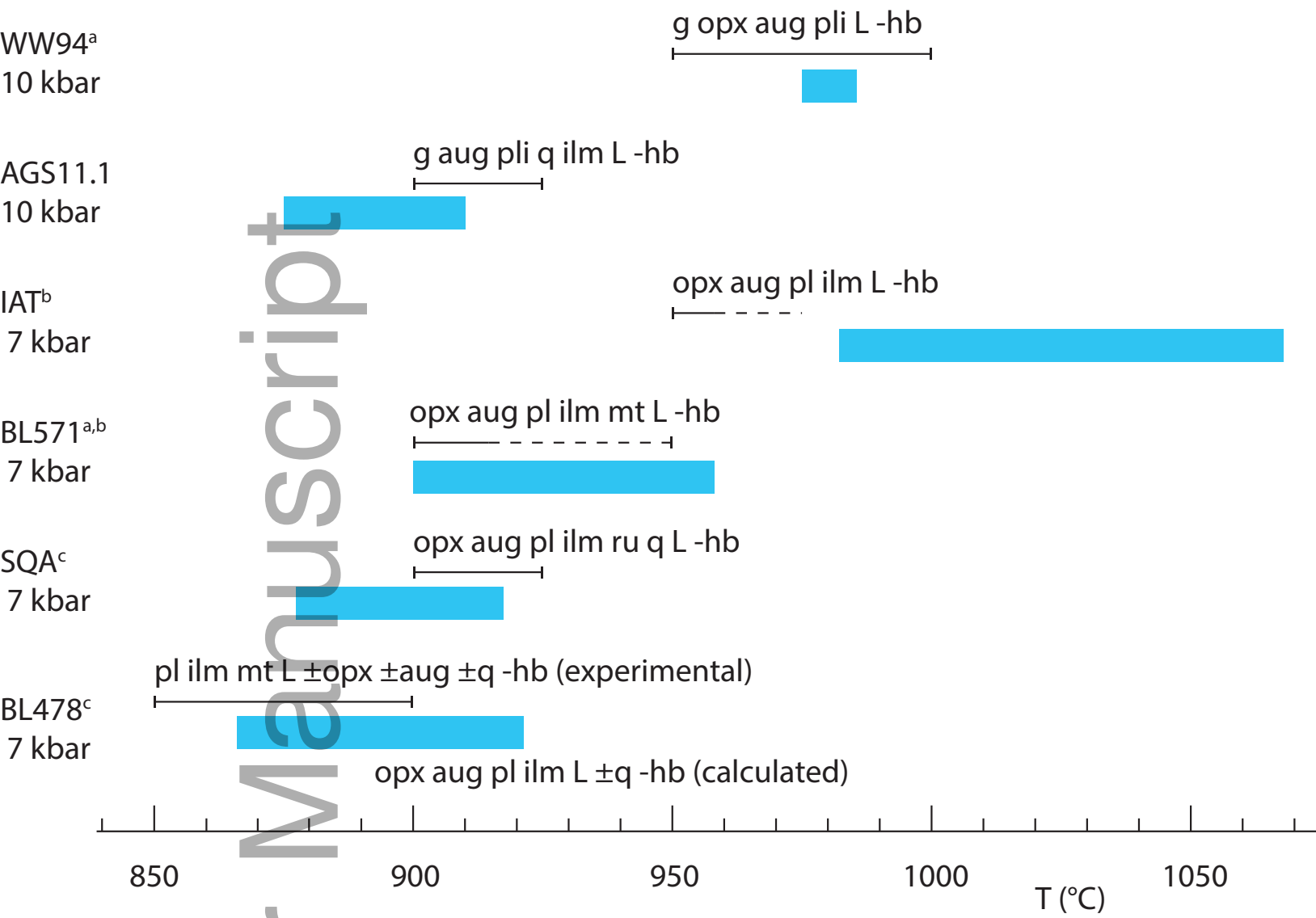


- 1) g o gl act law chl mu ru
- 2) g gl act law chl ep mu ru
- 3) g o gl act ep mu ru
- 4) hb chl ep mu ru
- 5) hb chl ep mu bi sph
- 6) hb ep mu bi ru sph
- 7) hb ep mu bi sph
- 8) o hb ep mu bi sph
- 9) o di hb ep bi sph
- 10) di hb ep bi sph
- 11) gl act chl ep bi ab sph
- 12) hb act chl ep bi ab sph
- 13) hb chl ep bi ab sph



This article is protected by copyright. All rights reserved





jmg_12211_f5.eps



Minerva Access is the Institutional Repository of The University of Melbourne

Author/s:

Green, ECR; White, RW; Diener, JFA; Powell, R; Holland, TJB; Palin, RM

Title:

Activity-composition relations for the calculation of partial melting equilibria in metabasic rocks

Date:

2016-12-01

Citation:

Green, E. C. R., White, R. W., Diener, J. F. A., Powell, R., Holland, T. J. B. & Palin, R. M. (2016). Activity-composition relations for the calculation of partial melting equilibria in metabasic rocks. *JOURNAL OF METAMORPHIC GEOLOGY*, 34 (9), pp.845-869.
<https://doi.org/10.1111/jmg.12211>.

Persistent Link:

<http://hdl.handle.net/11343/291668>

File Description:

Accepted version